Utrecht University

Institute for Subatomic Physics

Bachelor Thesis

D-tagged jet measurements in the ALICE experiment

Author
Wouter Huisman
Student number - 4164873

Supervisors
Dr. Barbara A. Trzeciak
Utrecht University
Dr. André Mischke
Utrecht University

June 14, 2017

Abstract

With the ALICE detector at CERN, scientists are studying the matter of the early universe in the laboratory. Nuclei are smashed onto each other, creating a new state of matter, called the quark-gluon plasma. The hot fireball that is created expands and cools down creating many particles that come in conical shapes called jets. ALICE measures these particles in order to study the quark-gluon plasma. One of these particles is the D-meson carrying information about the quark-gluon plasma transport properties. These jets contain many other particles than the D-mesons. Good simulation models have to be created in order to compare with the distorted data. In this thesis, proton-lead collisions at $\sqrt{s_{NN}} = 5.02$ TeV are studied, which provide a reference for the lead-lead analysis, in which the quark-gluon plasma is created. A model will be set up, which can be compared with data coming from ALICE. Modifications are applied on the model and the systematic uncertainties are assigned. The computational work was done using the ROOT and AliRoot frameworks.

Contents

Chapter 1

Introduction

1.1 The Standard Model

'By convention there is color, by convention sweetness, by convention bitterness, but in reality there are atoms and empty space.' (Democritus, circa 400 BCE). As we know now, Democritus was on the right path and far ahead of his time. Life around us consists of elementary building blocks. Splitting a grain of sand will result in a smaller grain of sand. But splitting these smaller pieces of sand will eventually lead to something that cannot be split any further. Democritus called these particles 'atoms', after the Greek word *atomos*, meaning 'that which cannot be split'. As we know now, atoms are not the smallest building blocks of matter. There exists a whole new world in the regions smaller than atoms: *the subatomic world*. Physics research, with the help of particle accelerators, revealed the wide spectrum of the subatomic world. In order to explain how the particles make up the essential building blocks of matter, physicists described these particles in a universal model called *The Standard Model of Particle Physics* (figure 1.1). From this Standard Model, we can divide our world into different particles: *fermions* and *bosons*. Fermions are quarks and leptons. Gauge bosons are the force carrier particles, i.e. the photon carrying a force between two interacting charged electrons.

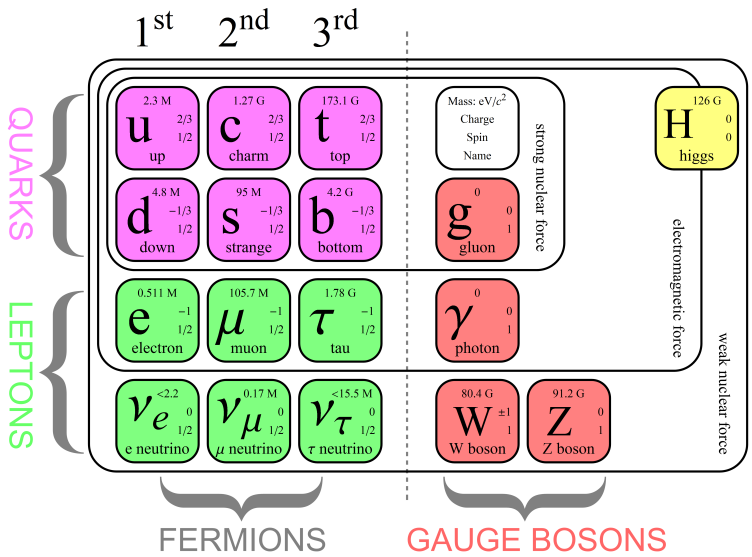

Figure 1.1 – The Standard Model of Particle Physics, with each of the fundamental forces linked to force carrier bosons. There are 6 different 'flavours' of quarks: up, down, charm, strange, top, bottom. Ordinary matter (protons and neutrons) consists of only the up and down quark [1].

The Standard Model describes three different interactions. The best known being the electromagnetic interaction, which describes the interactions between electrically charged particles. The weak nuclear interaction is responsible for nuclear decay, and whose fundamental process is transforming a proton into a neutron, an electron and a neutrino. The strong nuclear interaction is responsible for holding most ordinary matter together because it confines quarks into *hadrons*, such as protons and neutrons. The interaction length of the strong interaction is very short (10^{-15} m), but has a relative high interaction strength compared to the other fundamental interactions. Gravitation is not described by the Standard Model, as the force carrying particle, the *graviton*, has not yet been discovered [2].
Force carriers are particles that carry a force between different interacting fermions. The interaction between i.e. two negatively charged electrons can be visualized as one electron emitting a virtual photon, which gets absorbed by the other electron, causing a momentum transfer between the electrons. A virtual particle exhibits some of the characteristics of ordinary particles but it is a transient fluctuation whose existence is limited by the uncertainty principle [3]. Photons are the force carriers of the electromagnetic interaction. The W and Z bosons, are the force carriers of the weak interaction. And finally, the *gluon* is the *strong force* carrying particle. In the case of the strong interaction, the particles (quarks and gluons) are called *partons*.

1.2 Quantum Chromodynamics

As mentioned before, the strong interaction is responsible for holding ordinary matter together. The theory describing the strong interaction is called *Quantum Chromodynamics (QCD)*. QCD describes the behaviour of quarks and gluons, the building blocks of hadrons: *baryons* and *mesons* [4]. Mesons are intermediate mass particles, which are made up of a quark anti-quark pair (i.e. $c\bar{u}$). Three quark combinations are called baryons (i.e. uud). Mesons are bosons (though not force carriers as the four gauge bosons), baryons are fermions [5]. QCD started with the idea that hadrons consisted of even smaller particles. Quarks were proposed, which would interact with each other through gauge bosons, called gluons. High-energy collision experiments revealed the substructure of hadrons through *deep inelastic scattering* of electrons on protons carried out at the Stanford Linear Accelerator Center (SLAC) [4].

Theory proposed that quarks move within the nucleons at nearly the speed of light. The force keeping the quarks confined to the nucleus must be rather large to account for this. Individual quarks and gluons were never detected, but experiments revealed the substructure of hadrons. How can there be a force strong enough to confine the quarks in the nucleons but weak enough to be detected by collision experiments? *Gross*, *Politzer* and *Wilczek* (awarded the Nobel Prize in 2004) provided the answer, called *asymptotic freedom*. This is the property that at distances around the size of a nucleon (10^{-15} m) the attraction between quarks large enough to keep them confined to the nucleon. But at distances shorter than that, explored in high energy collisions, the attraction is weaker [6]. The physical concept can be visualized using an elastic string which holds the particles together (figure 1.2). When the particles are pulled apart, the string pulls them back together. If the particles are close together, not much of a force is applied in the string. But if so much energy is used to pull the quarks apart, the string can brake and form new quarks and anti-quarks using the released energy, resulting into new hadrons. The strings in this illustration can be thought of as the gluons interacting with the quarks and holding them together as mentioned in the previous section. It was proposed that quarks had another degree of freedom called *color charge*. Color charge of quarks is similar to electrical charge in a sense that an equal number of positive and negative charges results in a neutral net charge, and in the case of color charge, the particle is color neutral. There are three colors and anti-colors: (anti-)red, (anti-)blue and (anti-)green. All mesons ($\bar{r}r, \bar{b}b, \bar{g}g$) and all baryons ($\bar{r}\bar{g}\bar{b}, rgb$) are color neutral [7]. Gluons consist of a combination of 8 different color states. The color singlet state, where the gluon is color neutral, and the color octet state where the gluon consist of a combination of two colors and its anti-colors. The most striking feature of QCD is the *color confinement*. Color

confinement means that color charged particles, such as quarks and gluons cannot be isolated as separate objects [4].

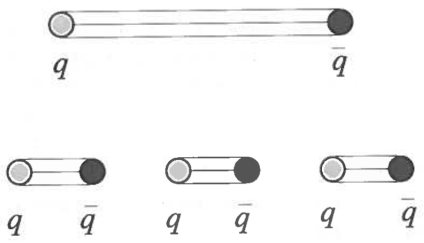

Figure 1.2 – Schematic view of the confinement mechanism. As the quarks are pulled apart with high enough energy, the string breaks and new quark anti-quark ($q\bar{q}$) pairs are formed [4].

1.3 Quark-Gluon Plasma

The *Big Bang Theory* is the prevailing theory for describing the evolution of our universe. It offers insight in the expansion from a very hot and dense state into the current large scale, cold state of our universe. It also offers a comprehensive explanation for a broad range of phenomena including the abundance of light elements, microwave background, large scale structure and Hubble's Law [8]. In the early stages of the universe, around a microsecond after the Big Bang, the universe undergoes rapid expansion. The universe cools down to below 10 quadrillion degrees (10^{15}) while quarks electrons and neutrinos form in large numbers. The four fundamental forces (strong, weak, electromagnetism and gravity) take their present form and the still very hot and dense 'soup' forms a *quark-gluon plasma (QGP)*. The quark-gluon plasma then further cools down and quarks rearrange themselves into *nucleons* like protons and neutrons. The protons start capturing free electrons, creating hydrogen atoms. Larger elements like helium start to form and the universe becomes transparent to light as it expands. Small dense clouds of cosmic gas collapse under the growing influence of gravity and stars, planets and galaxies form [9]. At this point in time, we have arrived at the current state of the universe (figure 1.3 shows schematically the evolution of the universe).

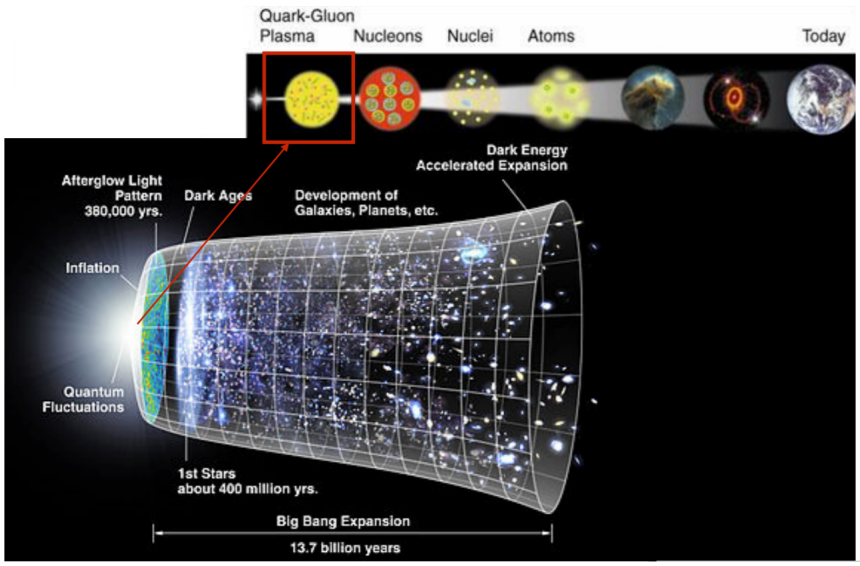

Figure 1.3 – Artist's interpretation of the schematic overview of the expansion of the universe [10].

Nowadays, the quark-gluon plasma can be created in the laboratory by high energy heavy-ion collisions. Studying the quark-gluon plasma enables the understanding of the very early stages of the universe. As mentioned before, at normal conditions (low temperature and/or density) quarks and gluons are confined in hadrons. However, at high enough temperature and/or density (as in the early stages of the universe), a phase transition may occur when ordinary hadrons no longer exist. This phase transition is called *deconfinement*. The quarks and gluons exist as free particles and form a quark-gluon plasma [4]. The quark gluon plasma expands and cools down, confining the quarks and gluons again in hadrons. Chapter 3 further describes the stages of heavy-ion collisions and the formation of the QGP.

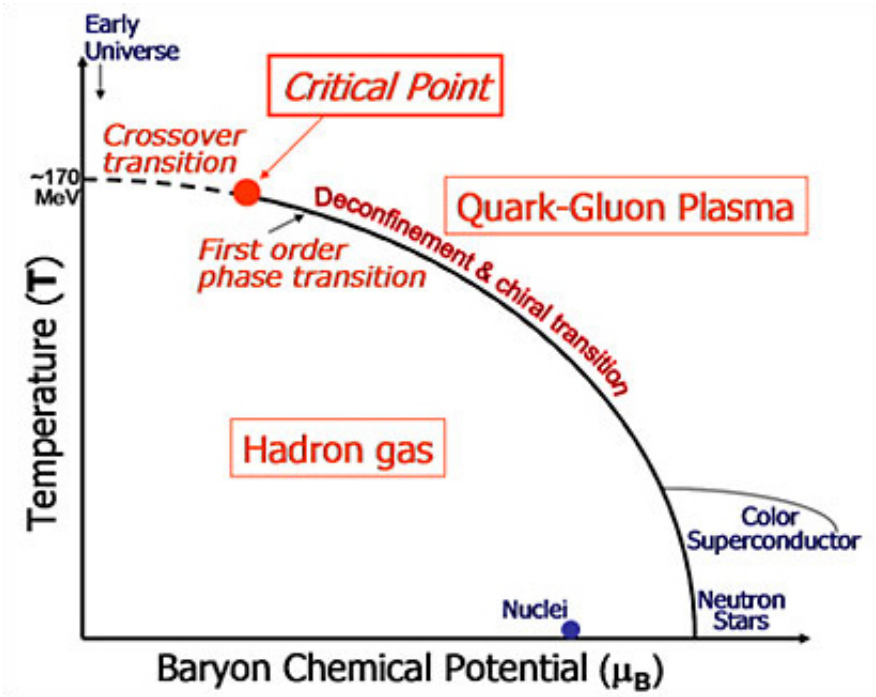

Figure 1.4 – Schematic overview of the QCD phase diagram. At low temperatures and/or baryon densities, the quarks and gluon are confined in hadrons. Deconfinement takes place when these parameters drastically increase. In particle accelerators, the baryon density is relatively low, where as the temperature is very high. In neutron stars, the temperature is relatively low but the baryon density is extremely high. It is suspected that a QGP also forms in neutron stars. [11].

Figure 1.4 shows a schematic picture of the QCD phase diagram. The crossover transition is pictured as a second order phase transition (continuous). If the phase transition were to be first order (discontinuous) a mixed phase consisting of the plasma and the hadron gas would be created. In such a case, one may consider three steps in the evolution of matter as it passes the phase transition. At first, to a good approximation, the matter is an adiabatically expanding QGP. Later the matter expands as a mixed phase of the plasma and the hadron gas and finally the matter expands as a hadron gas.

Chapter 2

Experimental setup

2.1 Large Hadron Collider

The Large Hadron Collider (LHC) on the border of Switzerland and France is the largest and most powerful particle accelerator in the world. It started in 2008 and remains the latest addition to the accelerator complex of CERN (Conseil Européen pour la Recherche Nucleaire). The LHC consists of a 27-kilometre ring of superconducting magnets with a number of accelerating structures to boost the particles up to velocities close to the speed of light. The particle beams travel in opposite directions in ultra-high vacuum before being collided with each other at extremely high energies. The electromagnets are built from coils of special electric cables that operates in a superconducting state, efficiently conducting electricity without resistance or loss of energy. This requires chilling the magnets to -271.3^{o}C, a temperature colder than outer space [12].

Figure 2.1 – Aerial photo of the LCH at CERN on the border of Switzerland and France. The different dots on the circle represent the different experiments [13].

At the LHC, there are four major experiments being conducted (figure 2.1). *ATLAS (A Toroidal LHC ApparatuS)* and *CMS (Compact Muon Solenoid)* are more general-purpose detectors who focus on the largest range of physics possible. *ALICE (A Large Ion Collider Experiment)* is specialized in focusing on heavy-ion physics [14] and *LHCb (Large Hadron Collider beauty)* is specialized in flavour physics. Since the research in this paper will be done in collaboration with ALICE, no further detail about the other

experiments will be given.

2.2 The ALICE detector

The ALICE detector is one of the main detectors of the CERN complex. The ALICE detector measures data from collision experiment produced by the LHC. ALICE specifically focuses on studying the early universe with the help of heavy-ion collisions at high energies. In these collisions, a quark-gluon plasma (QGP) forms, producing a number of particles, which the ALICE detector can measure. The ALICE detector is 25 meters long, 16 meters wide, and 16 meters in height. With a weight of 10000 tons, the ALICE detector weighs more than the Eiffel Tower. In figure 2.2, the shear size of the ALICE detector is clearly visible.

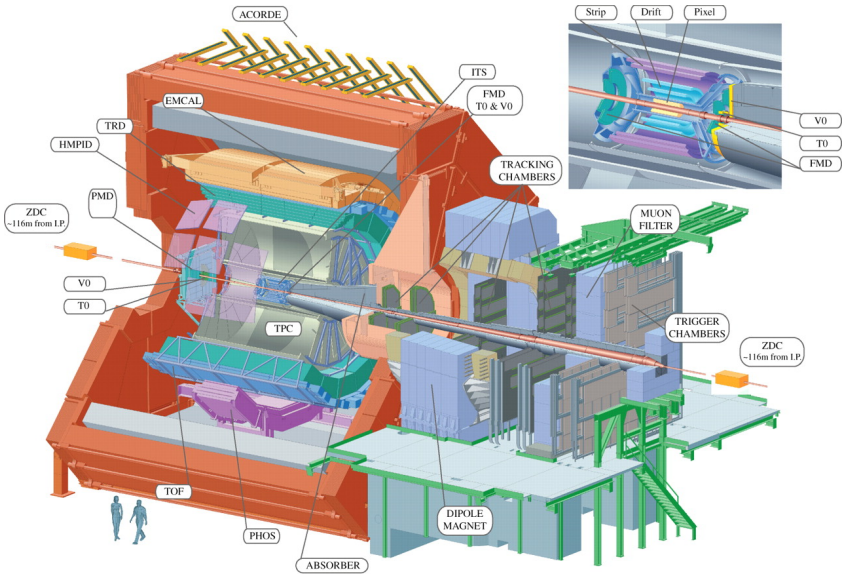

Figure 2.2 – Schematic view of the ALICE detector and its components [15].

Particle identification (PID) is the method of reading the information left by a passing particle through a particle to identify the particle. PID is used with many different detectors, with individual specializations. In the Large Hadron Collider at CERN, particles are collided at very high energies and detected using PID. The ALICE detector consists of several different systems to detect as many particles coming from the collisions as possible. The components which play a lead role in detecting the fragmented particles coming from the QGP will be discussed in sections 2.2.1, 2.2.2 and 2.2.3.

2.2.1 Inner Tracking System

The *Inner Tracking System (ITS)* is the detector closest to the primary interaction vertex (0.45 meter). It provides a high granularity and can measure the particles with high precision. It detects a number of particles, with the primary function to detect particles coming from weak interaction decays which contain a charm or a beauty quark. It consists of six concentric layers of silicon detectors: two layers of Silicon Pixel Detectors (SPD), two layers of Silicon Drift Detectors (SDD) and two layers of Silicon Strip Detectors (SSD). Figure 2.3 shows a close up of the detector and its components. Due to the high cost of precise measurement equipment, the choice for three different technologies was made. It keeps the ITS within a reasonable price tag by employing cheaper solutions as the required granularity decreases with the increase of the distance from the beam line. The SSD consists of two barrel layers of double-sided silicon strip detectors with analogue readout located at 436 and 385 mm from the beam line. The system contains 1698 sensors measuring 75×42 mm^2 each. The SDD contains two barrel layers of silicon strip at 238 and 149 mm from the beam line. The modules measure 75.3×70.2 mm^2. The SPD is

relatively the most costly of the 3 different technologies. It consists of two barrel layers of silicon pixel detectors at 76 and 39 mm from the beam line. Both layers will measure 286 mm along the beam direction. Each detector module consists of a two dimensional matrix of reverse-biased silicon detector diodes bonded to five readout chips. The readout is binary: a threshold is applied to the preamplified and shaped signal and the cell outputs a 1 if the threshold is exceeded [16]. The primary role of the ITS in ALICE is to improve primary vertex reconstruction, momentum resolution and Tracking and PID of low p_T particles.

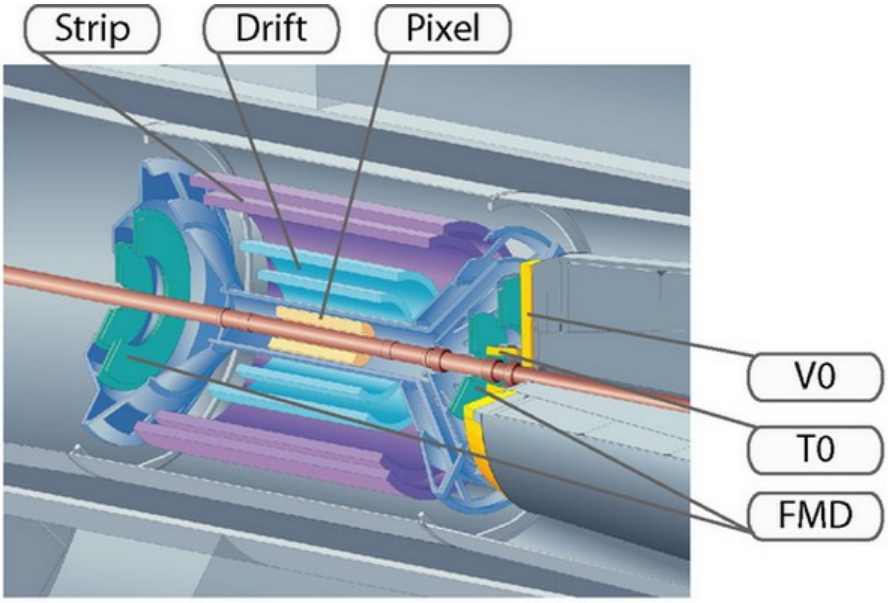

Figure 2.3 – Close up of the ITS in the ALICE detector. The ITS is the detector closest to the primary interaction vertex [16].

2.2.2 Time Projection Chamber

Time projection chambers (TPC), invented in 1974, give excellent spatial resolution in three dimensions and provide charge and mass information [17]. The TPC in ALICE is an 88 m^3 cylinder filled with gas and divided in two drift regions by the central electrode located at the beam axis centre. The field cage provides a uniform electric field along the z-axis. Charged particles passing through the TPC ionize the gas along their path, liberating electrons which then drift towards the end plates of the cylinder. The signal is them amplified through an avalanche effect in the vicinity of anode wires strung in the readout (see figure 2.4 for a close up of the detector and its components). Moving from the anode wire towards the surrounding electrodes, the positive ions created in the avalanche induce a positive current signal on the pad plane [18]. The TPC was designed to cope with the extreme instantaneous particle densities produced in heavy-ion collisions at the LHC.

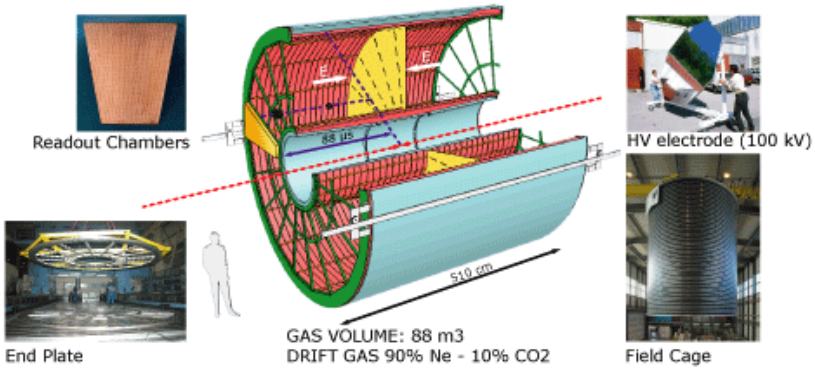

Figure 2.4 – Close up of the TPC in the ALICE detector [18].

2.2.3 Time of Flight Detector

Charged particles in the intermediate momentum range are identified in ALICE by the *Time Of Flight (TOF)* detector. Time measurement in combination with momentum and track length allows the TOF detector to calculate the particle mass. The detection method of the TOF looks quite similar to the method used by the TPC. The TOF detector is a stack of resistant glass plates on which a high voltage is applied on its external surfaces. Further out there are pickup electrodes. A charged particle ionizes the gas and the high electric field amplifies this ionization by an electron avalanche (figure 2.5 shows a charged particle passing through the detector). The resistant plates stop the avalanche development in each gap. However, they are transparent to the fast signal induced on the pickup electrodes by the movement of the electrons. The total signal is then the sum of the signals from all gaps. Many gaps equals high efficiency and narrow gap widths equals good time revolution. The detector element is a long MRPC (Multigap Resistive Plate Chamber) strip with an area of 7.4×120 cm^2. It has 96 readout pads of 2.5×3.5 cm^2 arranged in two rows. The modules in the TOF detector contain a total of 1638 detector elements (MRPC strips), covering an area of 160 m^2 with 157248 readout channels (pads) [19].

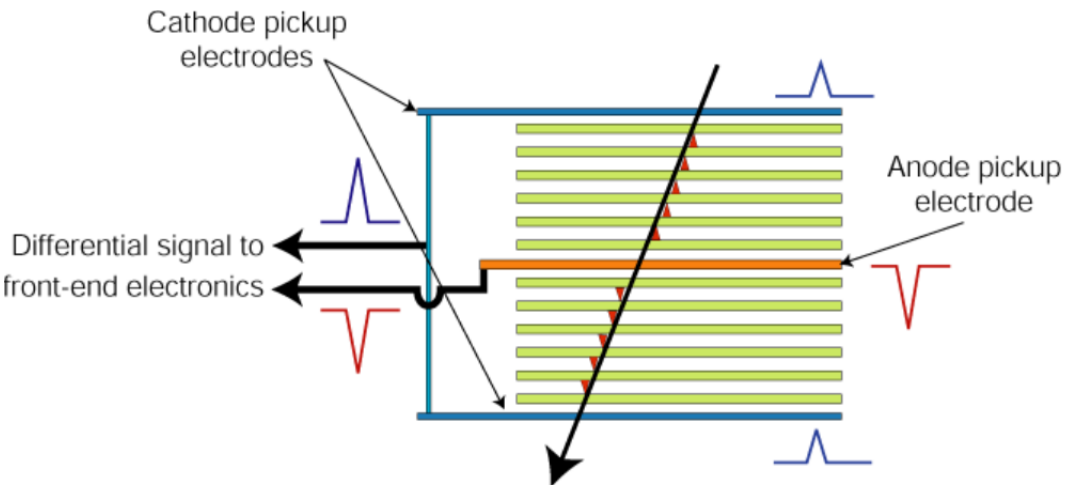

Figure 2.5 – A particle passing through the detector creating a trail of ionized particles, inducing an electric signal [19].

Chapter 3

Jets and D mesons

At the *Large Hadron Collider* (section 2.1) at CERN scientists are trying to recreate the conditions present at the early stages of the universe. By colliding particles with nearly the speed of light, the high temperature and baryon density in the collisions reach values similar to those at the early stages of the universe. Free quarks and gluons are created at the initial hard scattering of the collision, which then form a quark-gluon plasma. Quarks *fragment* (section 3.2) into countless particles, which are detected by ALICE. The great variety of particles are then measured and studied to provide information about the QGP. One of the emerged particles is the D meson, containing a heavy quark (*charm quark*) and a light quark. As we will see later on, the D meson is an important particle for the study of the QGP.
This chapter will be dedicated to discussing the production of jets from ultra-relativistic heavy-ion collisions. It will mention the different frameworks on how the jets form and will discuss the existence of D mesons within jets.

3.1 QGP production and evolution

In the high energy heavy-ion collisions at the LHC, nuclei are 'smashed' onto each other at nearly the speed of light. During these collisions, the baryon density and temperature are extremely high, reaching temperatures of 1.6 trillion $(10^{12})^o$C [20]. At these extreme conditions the nuclei cannot hold on to their substructure and evolve rapidly into an extended, hot and dense system of quarks and gluons. During the initial hard scattering process, new quark anti-quark pairs ($q\bar{q}$) may be created from the available energy (figure 1.2). These new $q\bar{q}$ pairs can be stretched further to create new $q\bar{q}$ pairs. These high momentum partons form a cascade, or shower. This cascade is called a *jet* [21]. Figure 3.1 schematically shows the collision and the formation of jets. There exist several stages in the evolution of heavy-ion collisions. These stages will be discussed in the following sections.

3.1.1 QCD string breaking

In the *string decay* picture, the nuclei pass through each other and the collisions of the nucleons lead to the formation of color strings like the ones depicted in figure 1.2. The strings then decay or fragment and form quarks and gluons or directly hadrons. The hadrons are modeled as smaller pieces of the original string [4].

3.1.2 QCD parton cacades

The *parton cascade model* views colliding nuclei as 'clouds' of quarks and gluons who penetrate through each other. Multiple hard scatterings between partons as well as the gluon radiation produce large energy densities. At low energies, the cascade model encounters problems, when the momentum transfers of parton scatterings are too small to be described by perturbation theory [4].

3.1.3 Color Glass Condensate

The *Color Glass Condensate* is referred to as the most complete and accurate theory until now. According to Einstein's theory of relativity, at high momenta, particles appear Lorentz contracted, or compressed along its direction of motion. Colliding particles then appear to be very thin sheets perpendicular to the beam axis (figure 3.1). The fast gluons are redistributed on the two very thin sheets. At very high energies, the gluon density inside the particles seems to increase dramatically. The gluons become closely packed together, and their interaction strength becomes weak. The word "color" comes from the property of color charge that the quarks and gluons posses. The word "glass" comes from the property of the closely packed gluons. Like glass, they behave as a solid on short timescales but as a liquid on long timescales. The word "condensate" comes from the high number of gluons. Immediately after the collision, longitudinal electric and magnetic fields are produced, producing a new state of matter called the *glasma* [4]. The glasma fields decay due to the classical rearrangement of the fields into radiation of gluons. The gluons thermalize with quarks leading to the QGP formation. Figure 3.1 shows a schematic representation of the collision of the two sheets of nuclei, and the formation of the glasma.

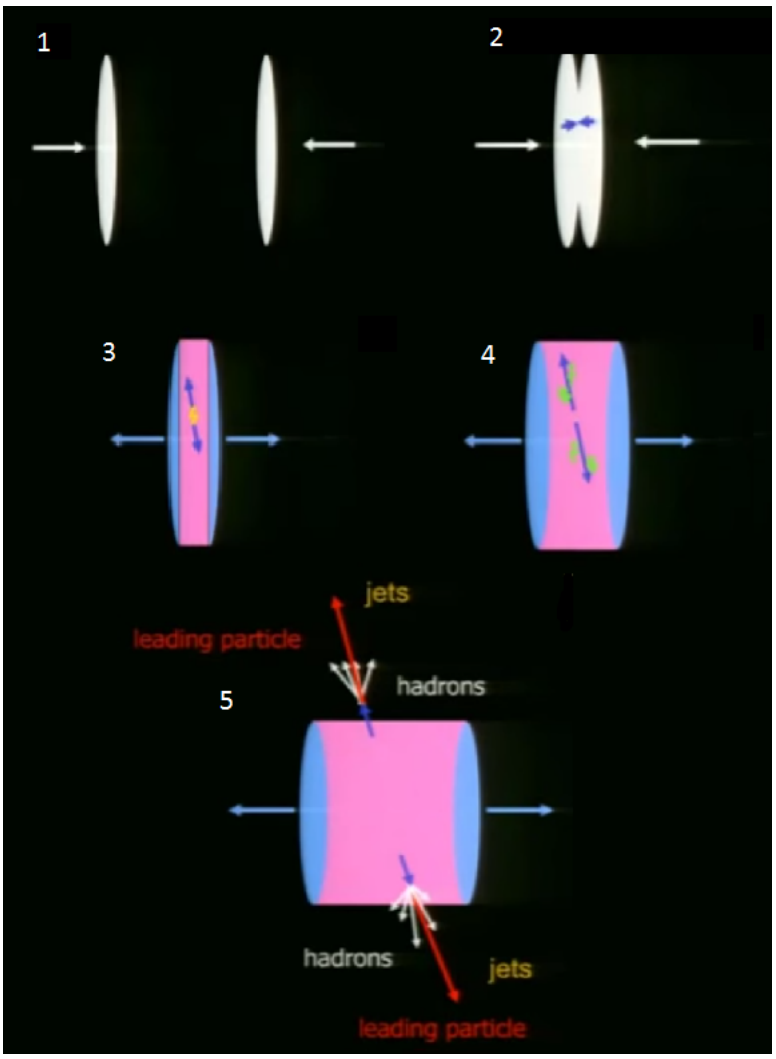

Figure 3.1 – Artist's representation of two colliding nuclei who are Lorentz contracted into two sheets. The colliding sheets produce a glasma which then transforms into the quark-gluon plasma, exiting jets of particles [4].

3.1.4 Thermalization and hydrodynamic expansion

During *thermalization*, particles reach thermal equilibrium due to interactions with each other. Any system naturally tries to increase entropy, going into a state of equipartition of energy (particles in thermal equilibrium have the same average energy). The equilibration is accelerated by instabilities generated in an anisotropic (directionally dependent) QGP [4]. If the thermalization rate is sufficiently fast, a locally thermalized QGP is created. The subsequent evolution of the system may be described by the equations of relativistic hydrodynamics, with small viscosity [4].

3.1.5 Hadronization and freeze-out

As the QGP cools down and expands. The quarks and gluons are confined again or fragment, to form hadrons. The partons form a jet, mentioned in section 3.1, which then evolves into a hadron jet. The process of confining quarks and gluons into hadrons is called *hadronization*. Figure 3.1 schematically shows this process. As the hadronic system expands, its baryon density and temperature decrease while the mean free path of the particles increases. At this point the particles can move freely to the detectors. This part in the evolution of matter is called the *thermal freeze-out*. In this case the measurement of the transverse-momentum spectra reveals information about the state of matter just before the thermal freeze-out [4]. The freeze-out is a stage in the evolution of matter when the hadrons stop interacting with each other. There are two kinds of freeze-outs: *thermal freeze-out* and *chemical freeze-out*.
Chemical freeze-out may take place before the thermal freeze-out. At low colliding energies, the inelastic cross sections are typically smaller than the elastic cross sections. Therefore, as the hadronic system cools down the inelastic collisions between its constituents are very likely to cease before the elastic collisions. The moment when the inelastic collisions stop is defined as the chemical freeze-out. As the system evolves from the chemical to the thermal freeze-out, the dominant processes are elastic collisions and strong decays of heavier resonances which populate the yields of stable hadrons [4]. The space-time diagram of the ultra-relativistic heavy-ion collisions is schematically shown in figure 3.2.

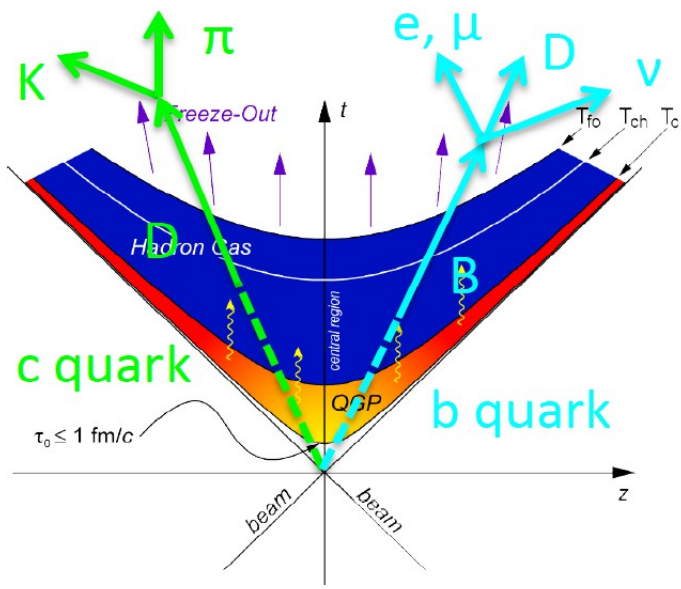

Figure 3.2 – The space-time diagram of ultra-relativistic heavy-ion collisions. In the centre of mass frame, the particles moving fast, hadronize later than those moving slowly [22].

3.2 D mesons

There are six different quarks shown in figure 1.1: up, down, charm, strange, top and bottom. These are referred to as quark 'flavours'. Ordinary matter consists of only two different flavours: up and down. These are the lightest of the quarks. These quarks make up the protons and the neutrons which are the building blocks for atoms that make up all the matter we see around us (figure 3.3).

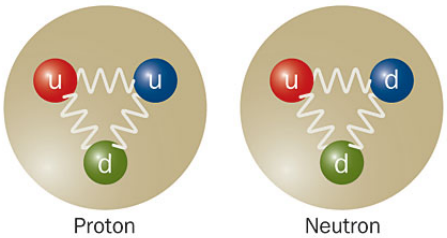

Figure 3.3 – Up and down quarks confined in proton and neutrons, which are color neutral (rgb) [23].

Heavy flavour quarks (c, t, b) are produced during hard scattering processes in heavy-ion collisions, according to the mass-energy equivalence ($E = mc^2$). These quarks, which interact with the QGP, may then fragment into a heavy flavour hadron called a *D meson*. The D meson is a particle, which contains a heavy flavour quark (c-quark) and a light quark ($D^{*+} : c\bar{d}$, $D^{*-} : d\bar{c}$). As the QGP is produced and evolves (section 3.1) the heavy-flavour quarks propagate through the QGP medium, losing energy by interactions (radiation induced energy loss induced by the QGP medium and collisional energy loss), thus providing information about the QGP transport properties. The D meson then, just like its constituent (the c-quark), also carries information about the QGP transport properties.
This fragmentation from a c-quark happens via *prompt* D meson production ($c \rightarrow D^{*\pm}$). Due to large masses, heavy-quarks are dominantly produced in the initial hard scattering stage of the collision. In the case of heavy flavour, the fraction of a partons momentum carried by the final hadron is much larger than in the case of light hadrons, which is why D mesons are a good proxy for determining the c-quark kinematics. Detection of a D meson could provide information about the QGP. Direct detection of a D meson however is not possible, since it has a very short lifetime ($\sim 10^{-13}$ s). That is why, in collision experiments, the decay products are detected. D mesons decays via the following decay channels [24]:

$$D^{*\pm} \rightarrow D^0 + \pi^{\pm}, BR = 67.7 \pm 0.5\%, \tag{3.2.1}$$

$$D^0(\bar{D^0}) \rightarrow K^{\pm} + \pi^{\mp}, BR = 3.93 \pm 0.04\%, \tag{3.2.2}$$

where BR is the *branching ratio*. D mesons may be produced in various different ways.

Fragmentation Fragmentation is the process where a particle continuously fragments into an increasing number of particles. In this case specifically, a high energy parton, which fragments into a parton jet, which in turn fragments into a hadron jet. A c-quark can fragment directly into a D meson via *prompt* D meson production ($c \rightarrow D^{*\pm}$).

Gluon splitting Gluon splitting is the process where a gluon decays into a quark and an anti-quark, just like in the string decay model. Normally, only light quarks are produced this way, but if the energy if high enough (i.e. at high energy collision experiments at the LHC), heavy-quarks like the c-quark may form.
D mesons containing c-quarks originating from the initial hard scattering are expected to carry a larger fraction of the total jet momentum as compared to those where the charm content arises later in the jet [24]. These D mesons originating from gluon splitting do not provide information about the QGP transport properties, since the c-quarks are formed

after the initial hard scattering process. What we measure from these quarks might not be quark energy loss but gluon energy loss. Its exact contribution is not well explored and is still not known.

Low p_T coalescence D mesons can also form through coalescence of a low p_T c-quark with a light quark formed during the QGP. Coalescence D mesons are not produced from direct fragmentation but do provide information about the QGP energy loss. The spectra however is shifted since these D mesons do not really form a jet. The fraction of these kind of D mesons is expected to be rather low.

Decay from B mesons Just like c-quarks are formed during hard scattering processes, a b-quark may similarly be formed. A b-quark originating from the initial hard scattering may fragment into a B-meson. This B-meson then decays into a D meson. D mesons can thus originate from either a c-quark, or B-meson decay. This is called *prompt* (c→D) and *non-prompt* (b→B→D) production.

3.2.1 Heavy-quark transport properties of the QGP

Quarks propagating through the QGP interact with the medium in two different ways. Medium induced inelastic energy loss is called *radiation induced energy loss*. This means that the quarks lose energy by emitting radiation in the form of gluons. The energy loss is color charge and quark mass dependent. Gluons are expected to lose more energy than quarks. The quark mass dependence of this energy loss leads to the *dead cone effect*. The radiation from quarks with mass m_q and energy E_q is suppressed for emission angles $\theta < m_q/E_q$. The higher the quark mass, the less gluon energy loss is expected by so called 'gluonstrahlung', derived from the Bremsstrahlung occurring in the electromagnetic interaction. Figure 3.4 shows this process schematically.

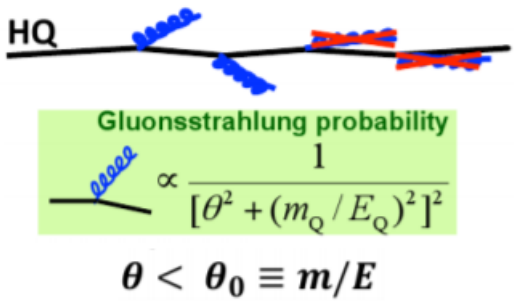

Figure 3.4 – A schematic view on how the propagating quarks emit gluons, via gluonstrahlung. At angles $\theta < \theta_0$ the gluons are not emitted. The more massive the quark, the larger this angle θ becomes, the less radiation induced energy loss the quark has [25].

The mass dependent energy loss of the different partons coming from the QGP is ordered in the following way:

$$\Delta E_{gluons} > \Delta E_{light-quarks} > \Delta E_{heavy-quarks} > \Delta E_{c-quarks} > \Delta E_{b-quarks}. \quad (3.2.3)$$

The other way quarks lose energy is through *collisional energy loss*. This means that quarks may collide with each other in the medium and thus lose energy. This energy loss is path-length dependent, since, the longer the path, the higher the probability that two quarks will collide.

Chapter 4

Analysis

As mentioned before, a jet is a group of particles emitted close to each other in momentum space. In an experiment, hadronic jets are measured, which are sprays of final state hadrons. These are produced after the freeze-out process. As mentioned in section 3.2, hadrons like the D meson, coming from fragmentation of heavy flavour quarks, carry a large part of the original partons momentum. D meson can originate from a c-quark or b-quark (B-meson decay). However, the D meson does not carry all of the partons momentum. D mesons are particles that travel inside jets along with other particles. By measuring the D mesons along with the surrounding particles in a jet from a c-quark fragmentation, we gain access to the original partons kinematics. The number of counts of the fragmented particles will be measured against transverse momenta (p_T). This will be done for both prompt and non-prompt D mesons. The main goal of this research is to study simulations of jets that contain D^* mesons. In this thesis, I will be specifically looking at jets, and D mesons within jets. Through simulation I will be able to assign and evaluate systematic uncertainties in the *D-tagged jet measurements* (jets that contain D mesons) and observe biases introduced by kinematic requirements on D mesons and jets in the data analysis. This will be done by applying analysis cuts on the p_T spectra. This chapter will be devoted to explaining the research that has been done and showing the results of the research.

4.1 Monte Carlo simulations

In order to create a good model, which later on can be compared with data, we need to run multiple simulations. Since there is no universal online database, which has perfect simulations for each different collision experiment, we have to construct one ourselves. In order to construct a good model for simulation, we need to introduce modifications in the model to evaluate the variations the modifications induce. This can be done by introducing different starting conditions or by applying analysis cuts in the p_T spectra (section 4.3). A dedicated *Monte Carlo* simulation was used for this analysis. This is a simulation technique where a physical process is repeated multiple times, with different starting conditions. The result is then a collection of simulations, which yields a cumulative distribution function that provides a whole range of possible outcomes. Usually, to describe prompt D meson spectra and the non-prompt fraction, FONLL calculations (Fixed-order next-to-leading logarithm) are used. In this analysis however, we need to have predictions for the prompt D meson spectra in jets and extract the *B feed-down* (subsection 4.1.1) as a function of the jet kinematics. Therefore this approach is not applicable. For this analysis we decided to use two Monte Carlo productions: POWHEG+PYTHIA6. POWHEG is a Monte Carlo event generator known to reasonably reproduce FONLL calculations and previous experimental results. PYTHIA6 (Perugia-2011 tune) provides the second part of the parton shower and the fragmentation into hadrons. In addition, a boost was applied in order to account for an asymmetric p-Pb collision system. We generated ∼25 million $c\bar{c}$ events and ∼25 million $b\bar{b}$ events for the default parameters $m_c = 1.5$ GeV/c^2, $m_b = 4.75$ GeV/c^2, $\mu_R = \mu_F = \mu_0 = \sqrt{m^2 + p_T^2}$, where m_c and m_b are respectively the masses of the charm and beauty quark and μ_R, μ_F are respectively

the *renormalization* and *factorization* scale factors. The default PDF is: CTEQ6 and the default nPDF is: EPS09NLO. These default values and modifications will be explained further in subsection 4.5.1.

4.1.1 Efficiency

The non-prompt simulation is corrected by an efficiency. The efficiency is calculated using different Monte Carlo simulations that have also a part related to the detector response. I implement there the same selection criteria as in data analysis to get the D meson in jets reconstruction efficiency. In order to compare simulation with data, we need to apply the ratio $\frac{Eff_{B\to D}}{Eff_{c\to D}}$ to the non-prompt simulation. We need to do this if we want to correct the data for the B feed-down (scaled non-prompt simulation) since we correct the inclusive data (prompt+non-prompt) at a point when it is corrected for prompt efficiency. The efficiency to the prompt spectra was not applied since the simulation will be compared with data that is already corrected for prompt.

4.2 Research questions

What are the systematic uncertainties for the D-tagged jet measurements? How do we evaluate them and how can they be limited? What are the kinematic biases we introduce by applying analysis cuts on jet spectra?

4.3 Selection criteria

4.3.1 Data

ALICE collects data from different collisions: proton-proton (p-p), proton-lead (p-Pb) and lead-lead (Pb-Pb). Theory predicts a QGP mainly at Pb-Pb collisions. The other collisions are done as a reference to the Pb-Pb collisions. The p-Pb analysis is an important step before looking at Pb-Pb because it is an intermediate step between p-p and Pb-Pb collisions. It important to check if there is no modification to effects, not related to the QGP. In this analysis, I will be looking only at p-Pb collisions at $\sqrt{s_{NN}} = 5.02$ TeV (centre-of-mass energy per nucleon pair). In data we need to apply selection criteria in order to get a signal. The reason to cut the data at certain p_T values can be explained by the D meson decay topology. The selection strategy is based on the topological displacement of the secondary vertex from the primary vertex due to their relatively large lifetime [24]. In the given data, there is also quite a lot of background noise. D meson candidates were selected as candidates based on the pion and kaon decay products. But this is a random combination of pions and kaons, and does not have to be decay products of D mesons. To reduce this, cuts were made in collision events.

PID of pions and kaons was performed using the information of the specific energy loss in the TPC and the time of flight provided by the TOF detector. In order to identify a track as a pion or a kaon its TPC $\frac{dE}{dx}$ (ionization energy loss) and/or time-of-flight were required to be within 3σ of the expected values. Tracks with no TOF information were identified using only the TPC. Tracks compatible with both the kaon and the pion hypotheses were retained for analysis and both mass hypotheses were considered [24].

4.3.2 Simulation

While looking at jet p_T spectra, the cuts were made in the D p_T spectra, and vice versa. If a cut is made in i.e. the D p_T spectra, no cut is made in the jet p_T spectra (the jet p_T spectra are cut at a wide range of 0-100 GeV/c). This is to ensure that the only bias we introduce is from cutting either jet p_T or D p_T spectra, but not both. In simulation, we can manually select the p_T range, which we want to evaluate. We cut p_T ranges in simulation in order to match the selection criteria used in data. This is called an *analysis cut*. This means that we will not look at particles traveling with a transverse momentum (p_T) outside this range. The analysis cuts are:

- Jet p_T distributions (cut in D p_T spectra)
  - Cut 0: (3-24 GeV/c)
  - Cut 1: (0-100 GeV/c)
  - Cut 2: (0-24 GeV/c)
- D p_T distributions (cut in jet p_T spectra)
  - Cut 3: (0-100 GeV/c)
  - Cut 4: (4-30 GeV/c).

4.4 Jet reconstruction

There are many ways of reconstructing jets. The standard protocol is to find the leading particle (high p_T hadron), and the particles close to it in momentum space. Since ALICE only measures particles and cannot measure the shape of the jets, algorithms are used to reconstruct the jets. Jet reconstruction algorithms are one of the main tools for heavy-ion collision analysis. The algorithms start with a number of measured particles and tries to associate them to jets, so that the kinematic properties of the jets can be related to the original parton created in the initial hard scattering stage. A jet algorithm has two major elements. The jet finding algorithm and the recombination scheme. The jet finding algorithm tries to group all the particles together in a jet. The recombination scheme tries to define how all the momenta of the particles in the jet are related, by combining them, to the original parton. Particles measured by ALICE are reconstructed into jets using the anti-k_T algorithm. This algorithm behaves like an idealized cone algorithm. A cone algorithm already assumes that the particles coming from the collision will show up in a conical shape [26]. Only charged particle tracks are used to reconstruct the jets.

4.5 Results

This section will only show part of the results obtained in the research. All the relevant information will be shown here, but for the sake of clarity, all the plots will be shown in appendices A and B. In this section, the prompt and non-prompt simulation results are shown for Cut 0 and Cut 4 with modifications applied. These will then be compared via ratio plots and further efficiency modifications.

4.5.1 Default parameters and modifications of simulation analysis

Simulation contains different starting parameters. In order to estimate the uncertainty, I applied modifications on these starting parameters. The modifications are made in the original quark mass, *renormalization*, *factorization* and *parton distribution function*.

Quark mass: Theory predicts the c-quark to have a mass of $m_c = 1.5$ GeV/c^2 and the b-quark to have a mass of $m_b = 4.75$ GeV/c^2. The modifications for the c-quark are: $m_c = 1.3$ GeV/c^2, $m_c = 1.7$ GeV/c^2. The modifications for the b-quark are: $m_b = 4.5$ GeV/c^2, $m_b = 5$ GeV/c^2.

Renormalization and factorization (μ_R and μ_F): Renormalization and factorization are modifications postulated in *quantum field theory* which describe probabilities in particle evolutions in time and space [27]. In this thesis, I will not go further into detail in quantum field theory. The default μ_R and μ_F is set to 1: $\mu_R = \mu_F = \mu_0 = \sqrt{m^2 + p_T^2} = 1$. Modifications are a different combination of factors 2 or 0.5 of the default value.

Parton distribution function (PDF): The parton distribution function (PDF) is a distribution function of the partons within nuclei. It describes the inner structure of nuclei, specifically, how the quarks and gluons propagate within the nucleon. They represent probability densities to find a parton carrying a momentum fraction x at a certain squared energy scale Q^2 [28]. The default PDF that was used is the CTEQ6LO. CT10NLO is the modification of this default PDF. For the case of p-Pb collisions, a *nPDF* is also used. nPDF stand for *Nuclear Parton Distribution Function*. This is because a PDF describes the distribution of partons in a nucleon, while a nPDF describes the distribution of partons in a nucleus (multiple nucleons) like the one of the Pb atom. The used nPDF is the EPS09 parton distribution function.

4.5.2 Prompt D* simulations

All the prompt D* distributions can be viewed in appendix B. In this section I will only discuss one jet p_T distribution cut and one D p_T distribution cut.

Cut 0: Jet p_T distribution In figure 4.1 we see the jet p_T distribution with the analysis cut on the D* spectra at 3-24 GeV/c. Since the jet cannot have a total momentum lower than the D meson inside it, we see the cut clearly visible at $p_T = 3$ GeV/c in the plot. However, the total jet momentum can be higher than the D meson momentum, so we do not see a clear cut in the jet p_T spectra at $p_T = 24$ GeV/c. The modifications discussed in subsection 4.5.1 are visible in this figure as the different variations. Each different color represents a modification on the default value (central value). As we can see, there is a visible spread between the variations on the central value. To make these variations more visible, I plotted them as a ratio with respect to the central value. This is visible in figure 4.2. The black dashed line in this figure represents the central value. As we can see in this figure, the ratios with respect to the central value differ up to 50%, where as the modification on the PDF shows a variation around 100%.

Cut 4: D p_T distribution Just like we looked at the jet p_T spectra, we also look at the D p_T spectra. This is done in figure 4.5. In this figure we see the D p_T spectra distribution with the analysis cut on the jet p_T spectra at 4-30 GeV/c. Since the upper limit in D momentum is limited by the upper limit in jet momentum (a D meson inside a jet cannot have a higher momentum than the momentum of the jet itself) we see a clear cut at $p_T = 30$ GeV/c. However, the D mesons inside a jet can have a momentum lower than the total jet momentum. This is the reason that we do not see a clear cut at $p_T = 4$ GeV/c. The modifications on the default values in the simulation are represented by the different variations with respect to the central value. The spread is made more visible by taking the ratio of the variations with respect to the central value. This is plotted in figure 4.6. In this figure we see the cut at $p_T = 30$ GeV/c again quite clearly. The variations with respect to the central value differ up to 50%, where as the modification on the PDF shows a variation around 100% or even higher.

4.5.3 Non-prompt D* simulations

All the non-prompt D* distributions can be viewed in appendix A. In this section I will only discuss one jet p_T distribution cut and one D p_T distribution cut. These cuts will be the same as the ones in the subsection about the prompt D* simulations.

Cut 0: Jet p_T distribution In figure 4.3 we see the jet p_T spectra with the analysis cut on the D p_T spectra on 3-24 GeV/c. In this figure we can clearly see the cut on the D p_T spectra at $p_T = 3$ GeV/c. We do not see the cut at $p_T = 24$ GeV/c clearly, since the jet momentum can be higher than the D meson momentum. The modifications are represented in the figure by the different variations with respect to the central value. The spread is made more visible by taking the ratio with respect to the central value. This is plotted in figure 4.4. In this figure we see that the spread is much lower than in the prompt jet p_T distribution spectra. The variations with respect to the central value differ up to 20%, where as the modification on the PDF shows a variation of around 40%.

Cut 4: D p_T distribution Just as we looked at the jet p_T distribution spectra, we also look at the D p_T distribution spectra. This is done in figure 4.7. In this figure we see the analysis cut on the jet p_T spectra at 4-30 GeV/c. We see the cut on the upper limit in the jet p_T spectra clearly (since a D meson inside a jet cannot have a momentum higher than the total jet momentum), where as we can also see on the other end of the spectra that D mesons can have a momentum lower than the total jet momentum. The different modifications on the central value are represented in the figure as the variations with respect to the central value. The spread is made more visible in figure 4.8 where the ratio with respect to the central value is taken. We see in this figure that the variations differ up to 20%, where as the modification on the PDF shows a variation of around 40%. At high p_T we see that the variations become rather large.

4.5.4 Prompt cut analysis

Comparing the different analysis cuts shows what biases we introduce on the simulation. In my research I used different simulation cuts to observe this. This subsection shows the different prompt analysis cuts.

Jet p_T spectra In figure 4.9 I plotted the jet p_T spectra central values of different analysis cuts (on the D p_T spectra) with respect to Cut 1: 0-100 GeV/c (which we can view as applying no cut on the spectra) and to Cut 2: 0-24 GeV/c. The different colors represent these different cuts. We see in this figure that, by applying cuts on the spectra, we bias the jet p_T distribution. We can see from the figure that, at low jet p_T ($p_T = 3$ GeV/c), we lose about 20% of D-jets when cutting the spectra on D p_T: 3-24 GeV/c. Also we lose D-jets at high p_T if we implement an analysis cut on the D p_T spectra. In the mid p_T ranges we see that we do not bias the simulation much with these analysis cuts.

D p_T spectra In figure 4.10 I plotted the D p_T spectra central value of Cut 4: 4-30 GeV/c by Cut 3: 0-100 GeV/c. These cuts were made in the jet p_T spectra. A cut of 0-100 GeV/c can be viewed as if no cut is applied. From this figure we can see that we lose about 60% of D-jets at $p_T = 4$ GeV/c, and start losing a lot of D-jets at $p_T > 15$ GeV/c.

4.5.5 Non-prompt cut analysis

Analogous to the previous subsection, I will show the different non-prompt analysis cuts.

Jet p_T analysis In figure 4.11 I plotted the jet p_T spectra central values of different analysis cuts (on the D p_T spectra) with respect to Cut 1: 0-100 GeV/c and Cut 2: 0-24 GeV/c. The different colors represent these different cuts. We see the bias on the p_T spectra that we introduce by applying analysis cuts. We lose about 30% of D-jets at low p_T when cutting the spectra on D p_T: 3-24 GeV/c. At high p_T we clearly lose less D-jets than is the case in the prompt cut analysis. If we cut the D p_T spectra at 2-36 GeV/c, we see the biases with respect to the D p_T cut at 3-24 GeV/c. At $p_T = 3$ GeV/c, we lose around 10% of the D-jets. At high p_T we lose less to no D-jets. In the mid p_T ranges we see that we do not bias the simulation much with these analysis cuts.

D p_T analysis In figure 4.12 we see that we bias the simulation a lot by applying an analysis cut. At low p_T (3 GeV/c) we lose around 50% of D-jets and start losing a lot of D-jets at $p_T > 10$ GeV/c.

4.5.6 Non-prompt and prompt comparison

Jet p_T spectra Figure 4.13 shows the comparison of prompt and non-prompt D mesons in jets at different p_T ranges for the jet p_T spectra. In this plot, both prompt and non prompt spectra are scaled by their cross-section. The way these distributions are calculated is: $\frac{Prompt\ Cut:\ X}{Non-prompt\ Cut:\ X}$. This is done for the three different cuts in the D p_T

spectra. From this plot we can see the connection between the ratio of non-prompt D mesons in jets and high p_T range. At low p_T, the ratio of non prompt over prompt D mesons in jets is around 10%, where as at high p_T this ratio is around 40%. We can see that applying a D p_T cut at 24 GeV/c that this influences the model, since at high p_T there will be a higher ratio of non-prompt over prompt D mesons in jets than if we apply no cut (0-100 GeV/c).

D p_T spectra In figure 4.14 we see the comparison between prompt and non-prompt D p_T distribution spectra for Cut 4: 4-30 GeV/c and no cut (0-100 GeV/c). If we apply no cut on the simulation, we see that at low p_T the ratio is around 5% of non-prompt over prompt D mesons in jets, where at high p_T this ratio is around 15%. By applying a cut in the jet p_T range, we bias the ratio of non-prompt over prompt D mesons. We see that at low p_T this ratio is around 12% and drops to 0% at $p_T = 29$ GeV/c. This is a strong bias we introduce in the simulation.

4.5.7 D meson fractions in jets

Prompt Figure 4.15 shows the number of counts that jets were found over a range of D meson fraction in jets. The fraction is calculated using: $frac = \frac{p_T^{D^*}}{p_{T,jet}^{D^*}} = z_\perp$. This figure shows that there are rather a lot of jets from which, a large fraction of jet p_T is carried by the D^* meson. Applying an analysis cut (D cut: 3-24 and jet cut: 4-30) greatly influences this. We see that without the cut (0-100 GeV/c) there is a smaller fraction of jet p_T carried by the D^* meson.

Non-prompt In the case of non-prompt production (figure 4.16) there are more jets with a high fraction of jet p_T carried by the D^* meson than in the prompt case.

4.5.8 Efficiency implementation

The reason to study simulation is so it can be compared with data from the LHC. Data coming from the LHC does not contain pure prompt (or non-prompt) D mesons, but rather a combination of the two. In order to get solely prompt data, we have to subtract non-prompt simulation (B feed-down) from the data, which we then can compare to prompt simulations. Before doing so, the non-prompt simulation needs to be scaled by efficiency. The efficiency is calculated using different Monte Carlo simulations that also have a part related to the detector response. We implement there the same selection criteria as in the data analysis to get the efficiency for the D meson in jets reconstruction efficiency.

Non-prompt I applied the ratio $\frac{Eff_{B\to D}}{Eff_{c\to D}}$ to the non-prompt simulation for Cut 0 (3-24 GeV/c). This is needed if I want to correct data for the B feed-down, since we correct inclusive data (prompt+non-prompt D mesons) at a point when this is corrected for the prompt D efficiency. Figure 4.17 shows the effect on efficiency scaling for non-prompt simulation clearly at low p_T.

Prompt I do not apply the efficiency scaling on the prompt spectra since we compare it in the end to data, which has already been corrected for efficiency.

4.5.9 Non-prompt B feed-down

B feed-down with variations As mentioned before, to compare data with simulation, we need to subtract the non-prompt simulation from the data to obtain a pure prompt data set, which we then compare with prompt simulation. This is done for non-prompt simulation for Cut 0 (D p_T cut: 3-24 GeV/c). The reason for taking Cut 0 is that data from ALICE was cut according to this spectrum, and simulation has to account for this. Figure 4.18 shows the non-prompt simulation for Cut 0. In this figure the simulation is rebinned in order to match data. It has been scaled by efficiency, cross-section and bin

width in order to be subtracted from data. This plot shows the cross section of Cut 0 over a p_T range, with the different modifications viewed as the variations with respect to the central value. In this plot is also the maximum variation with respect to the central value given as the thick band in the color teal.

B feed-down ratio with variations Figure 4.19 shows the ratios with respect to the central value for the non-prompt scaled simulation for Cut 0. The different variations are shown, as is the maximum spread in teal. The dashed line represents the central value.

B feed-down spread Figure 4.20 shows the non-prompt simulation for Cut 0 without the variations. The maximum spread is shown in teal and the central value is shown in black.

B feed-down ratio spread In figure 4.20 the maximum spread is viewed more clearly. The maximum spread is the teal band around the dashed black line which represents the central value. This band gives the systematic uncertainty per bin. The maximum spread is asymmetric around 1. The systematic uncertainty is then the largest of this spread. For example in the case for the bin 3-4 GeV/c, the systematic uncertainty would be 49%.

4.5.10 Systematic uncertainties

The systematic uncertainties on the non-prompt D*-jet simulations per bin for the simulation are given in table 4.1. This table shows the uncertainty from the up and down spread and the maximum uncertainty, which is the largest from the up or down spread. From this table it is clearly visible that the spread is asymmetric.

Table 4.1 – Table of all the uncertainties

B feed-down	Uncertainty (%)							
$p_T^{ch,jet}$ bin	3-4	4-6	6-8	8-10	10-12	12-16	16-24	24-40
Up	49	47	45	43	39	39	41	41
Down	43	39	35	31	29	25	24	25
Maximum	49	47	45	43	39	39	41	41

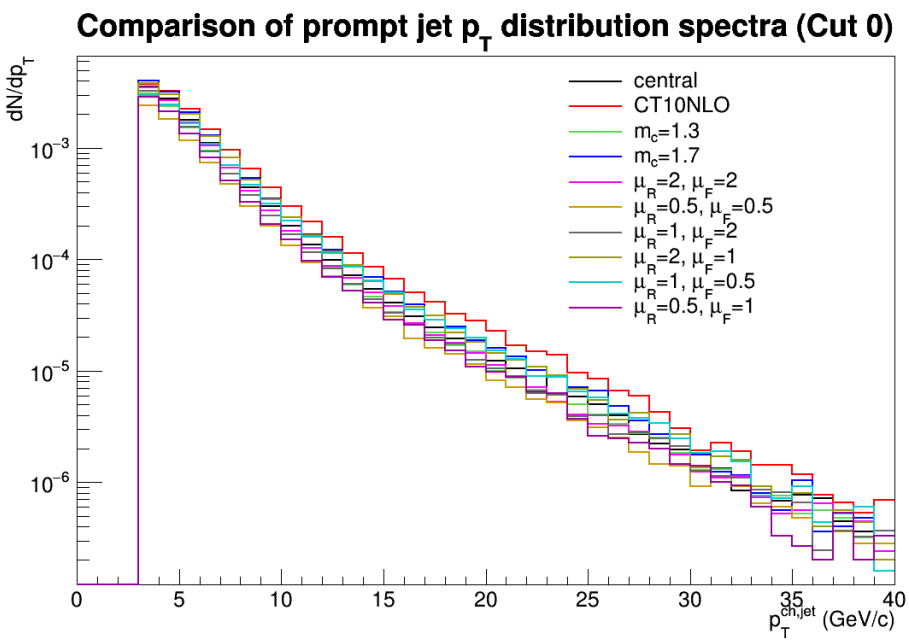

Figure 4.1 – Prompt jet p_T distribution plot for Cut 0 (3-24 GeV/c). Shown is the number of counts over a p_T range. The different colors represent the various modifications in the simulation. Since the jet cannot have a total momentum lower that the D meson inside it, we see the cut clearly visible in the plot. However, the total jet momentum can be higher that the D meson momentum, so we do not see a clear cut at $p_T = 24$ GeV/c.

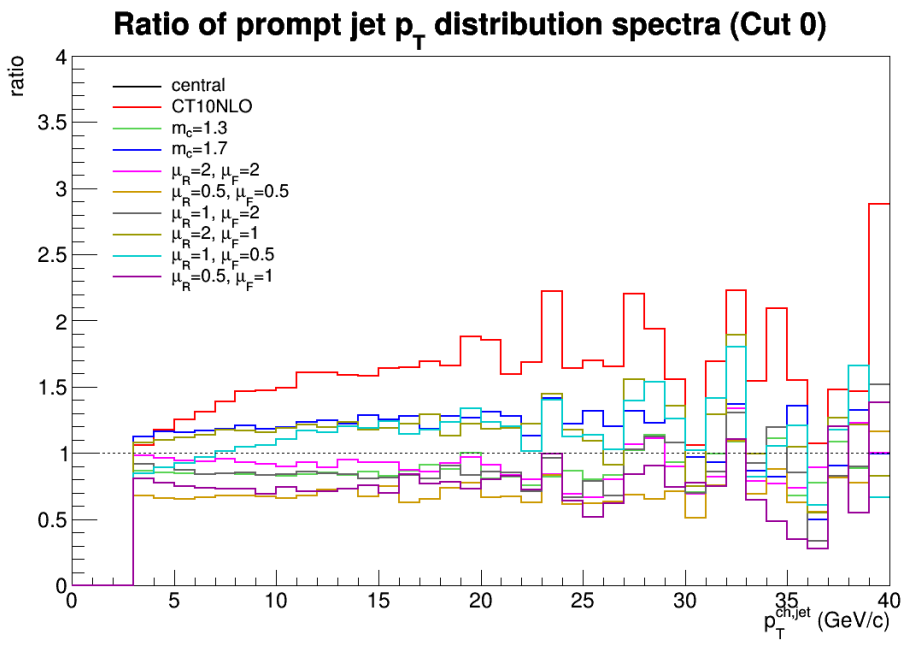

Figure 4.2 – Ratio of prompt jet p_T spectra with respect to the central value. The black dashed line represents the central value.

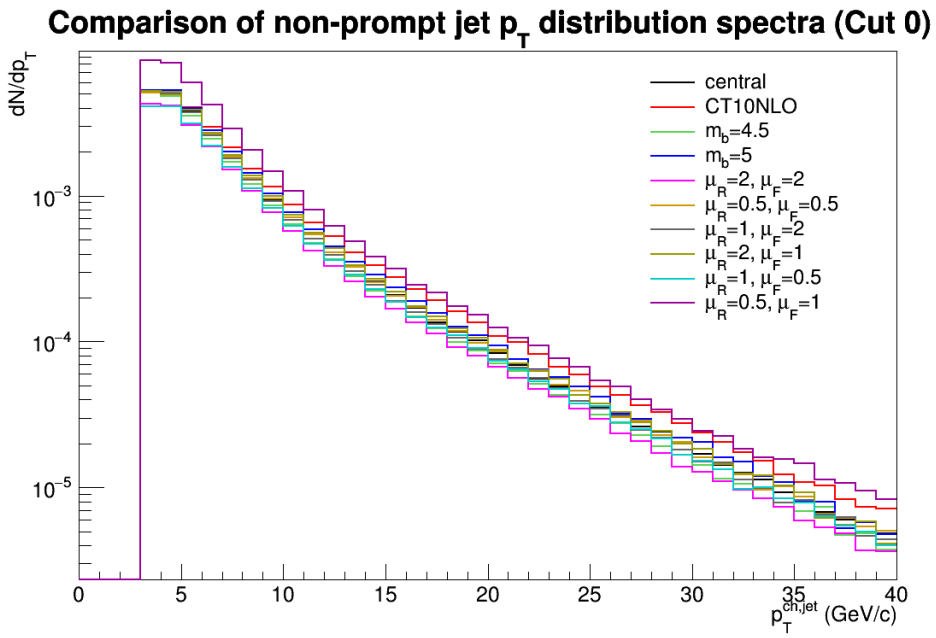

Figure 4.3 – Non-prompt jet p_T distribution plot for Cut 0 (3-24 GeV/c). Shown is the number of counts over a p_T range. The different colors represent various modifications in the simulation.

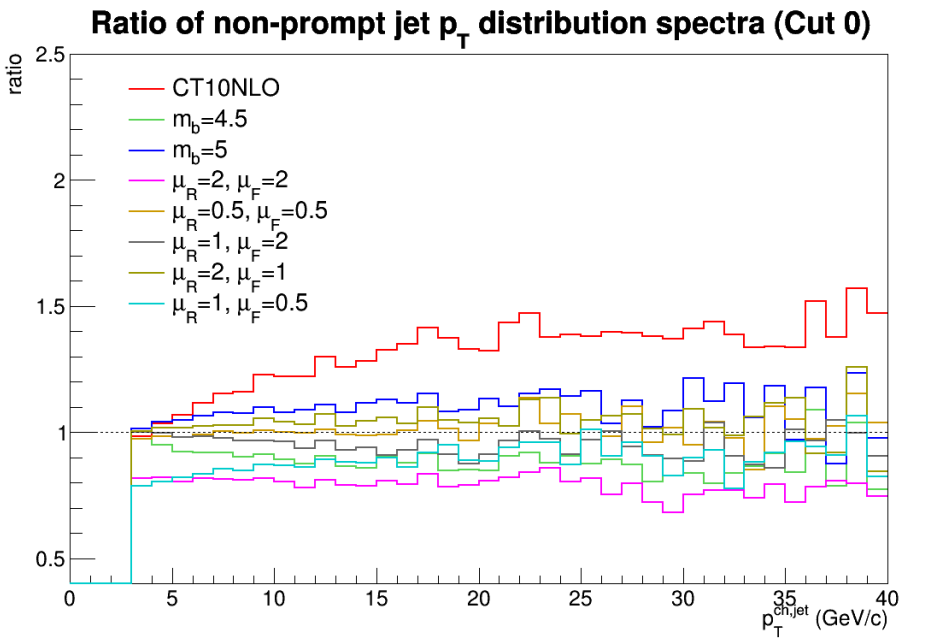

Figure 4.4 – Ratio of non-prompt jet p_T spectra with respect to the central value. The black dashed line represents the central value. It is clearly visible that the modifications on the central value cause a lesser variation in the simulation.

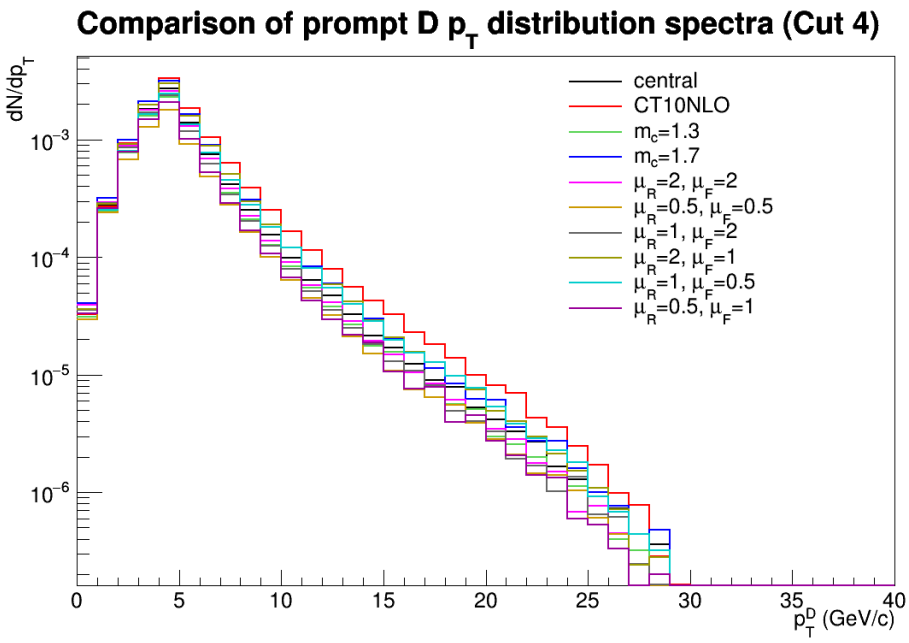

Figure 4.5 – Prompt D p_T distribution plot for Cut 4 (4-30 GeV/c). Shown is the number of counts over a p_T range. The different colors represent various modifications in the simulation. Here we cut the jet at 4-30 GeV/c. Since the D meson cannot have a higher momentum than the total jet momentum, we see the cut clearly visible at $p_T = 30$ GeV/c. However, the D meson can have a momentum lower than the total jet momentum, which we also see on the other end of the spectrum.

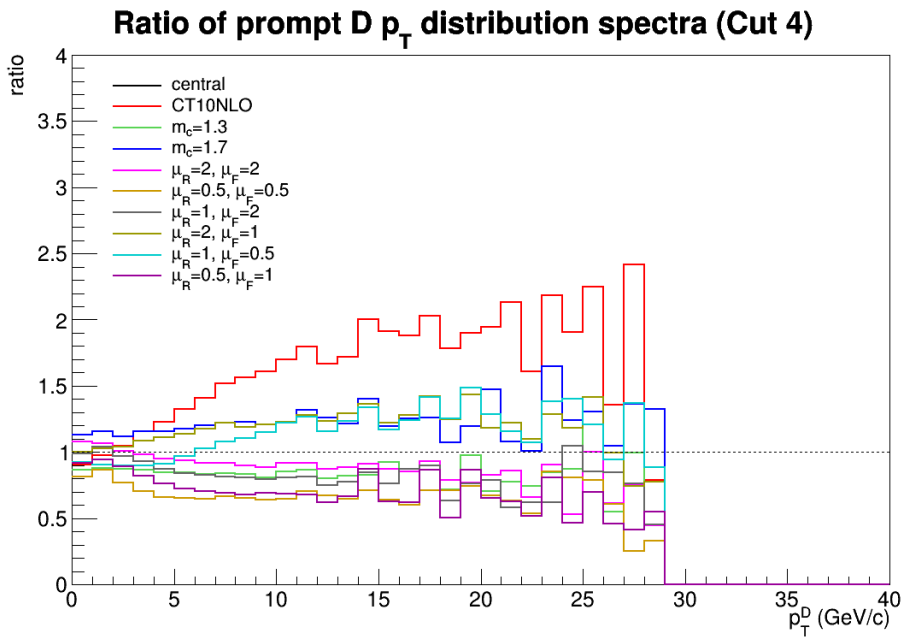

Figure 4.6 – Ratio of prompt D p_T spectra with respect to the central value. The black dashed line represents the central value.

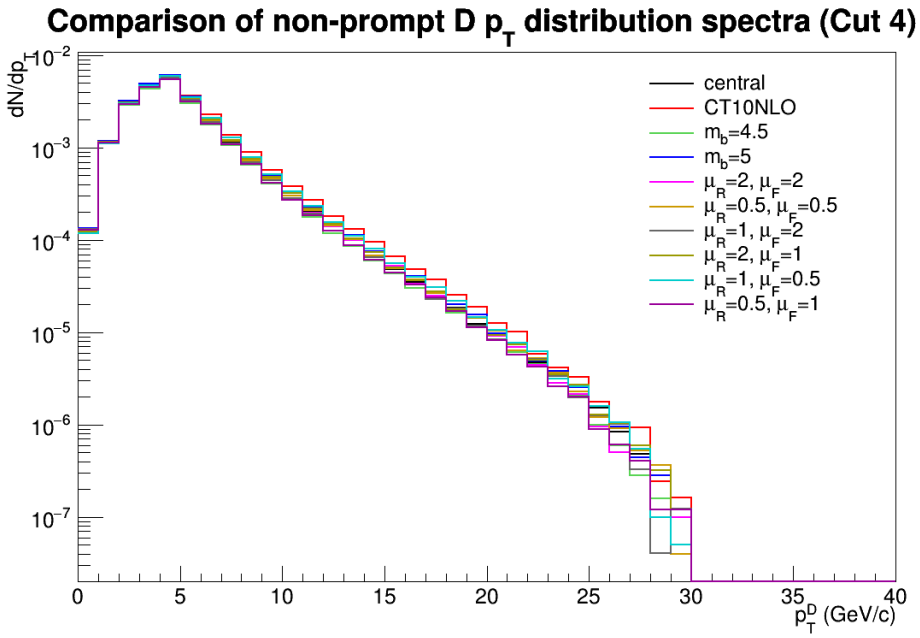

Figure 4.7 – Non-prompt D p_T distribution plot for Cut 4 (4-30 GeV/c). Shown is the number of counts over a p_T range. The different colors represent various modifications in the simulation.

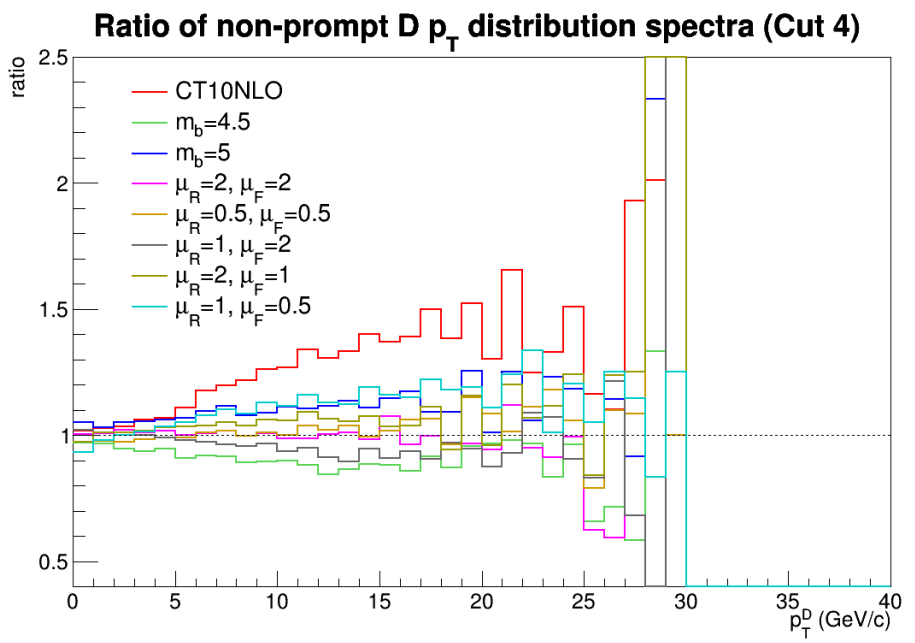

Figure 4.8 – Ratio of non-prompt D p_T spectra with respect to the central value. The black dashed line represents the central value. It is clearly visible that the modifications on the central value cause a lesser variation in the simulation. At high p_T however the variations become rather large.

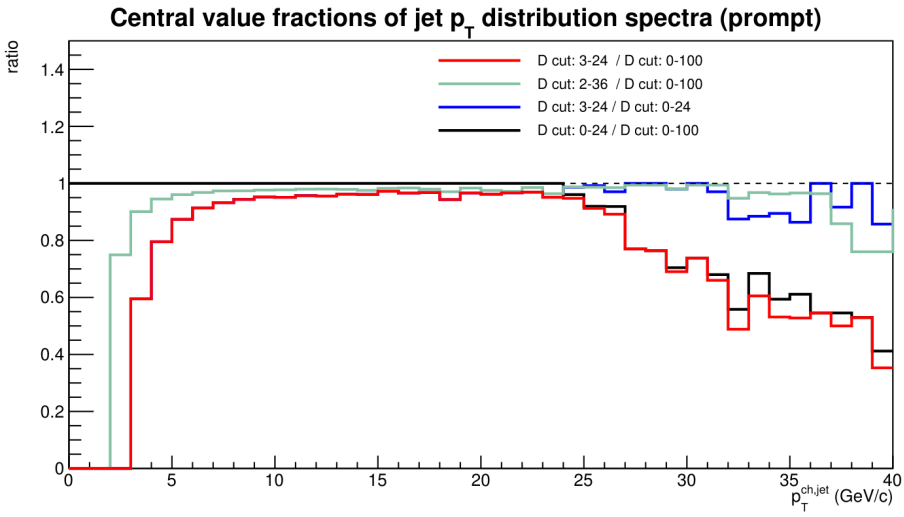

Figure 4.9 – Prompt central value ratios for jet p_T spectra with the different cuts in D p_T spectra.

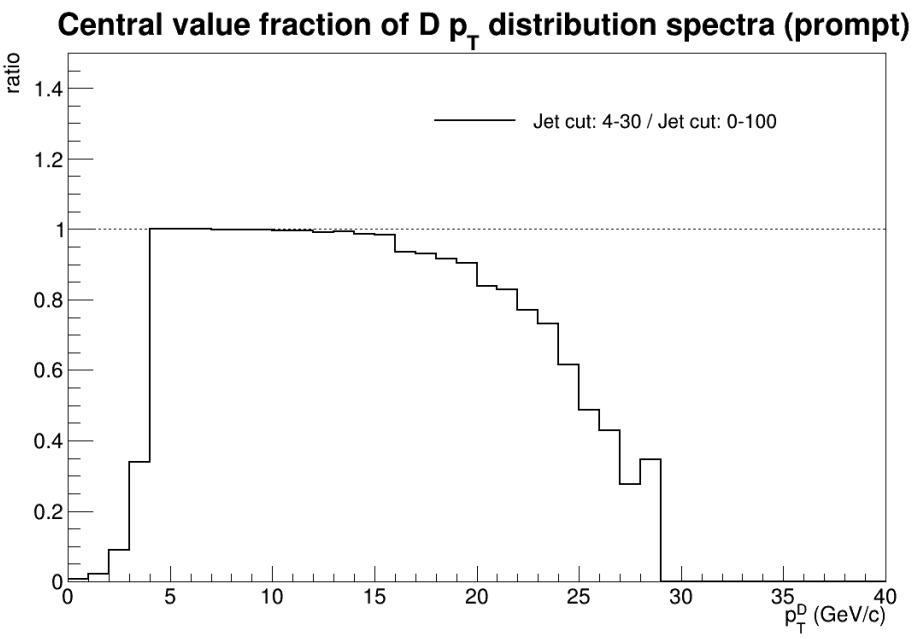

Figure 4.10 – Prompt central value ratios for D p_T spectra with the different cuts in jet p_T spectra.

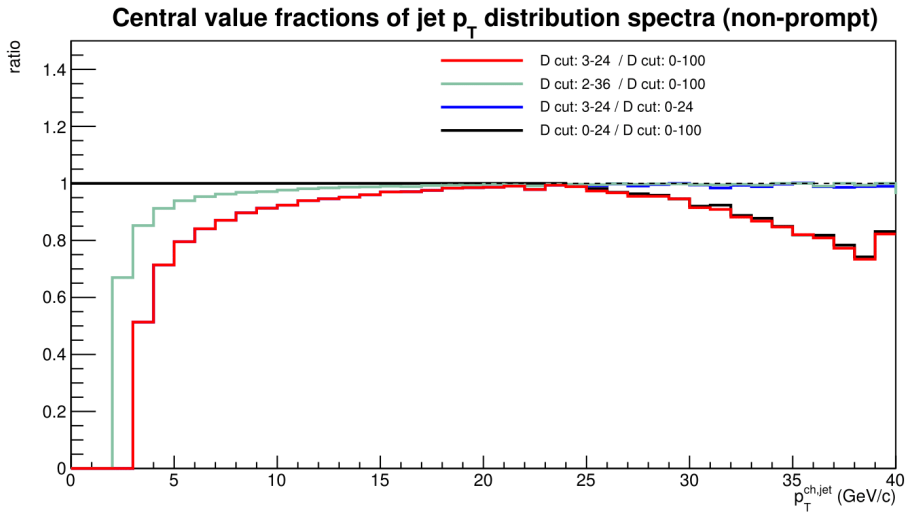

Figure 4.11 – Non-prompt central value ratios for jet p_T spectra with the different cuts in D p_T spectra.

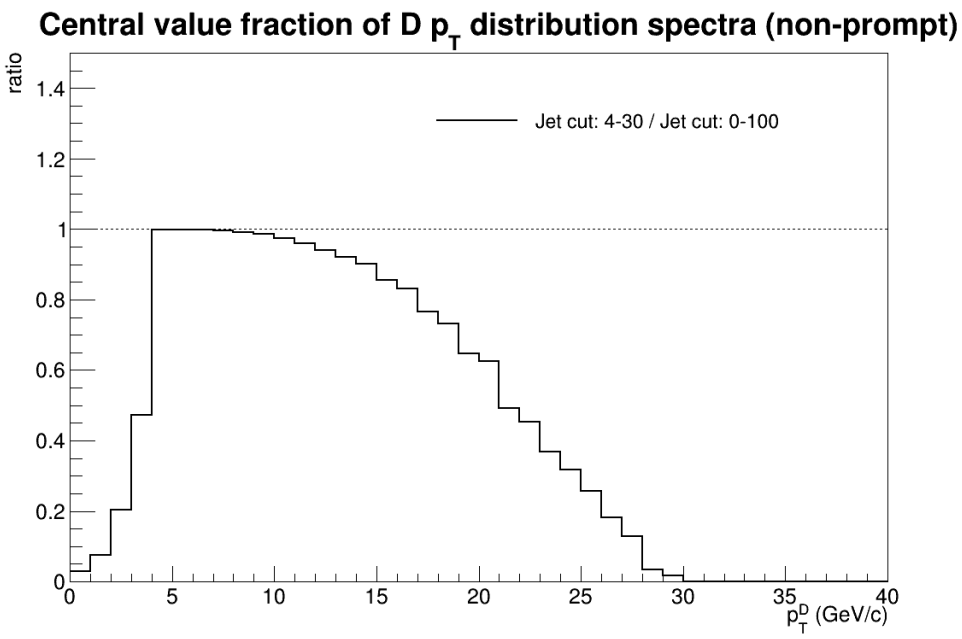

Figure 4.12 – Prompt central value ratios for D p_T spectra with the different cuts in jet p_T spectra.

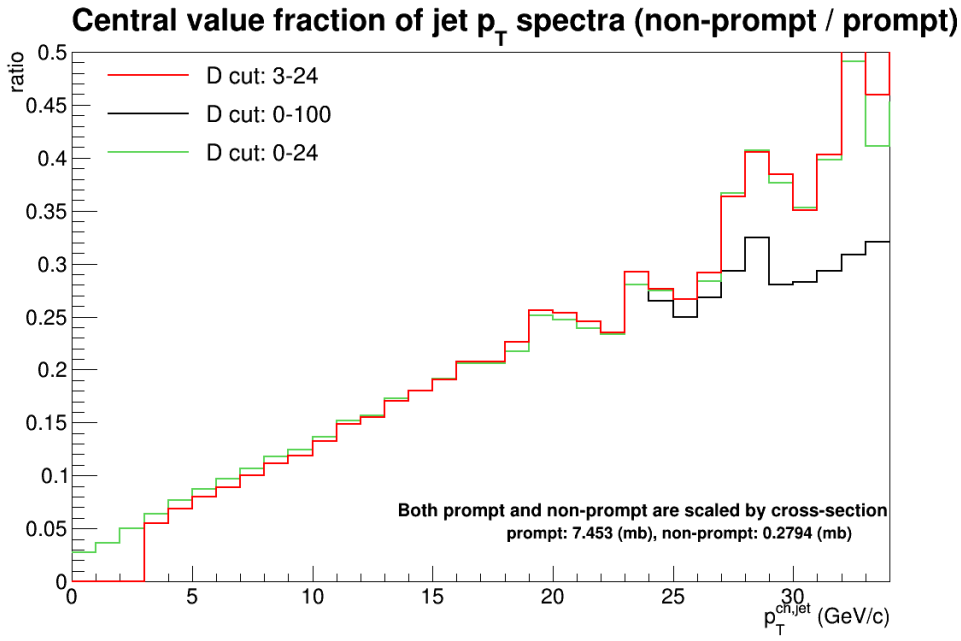

Figure 4.13 – Non-prompt versus prompt D meson production for central values of jet p_T spectra. Both prompt and non-prompt are scaled by their respective cross-section (in millibar). We see from this plot that at high p_T the ratio of non-prompt over prompt D mesons increases.

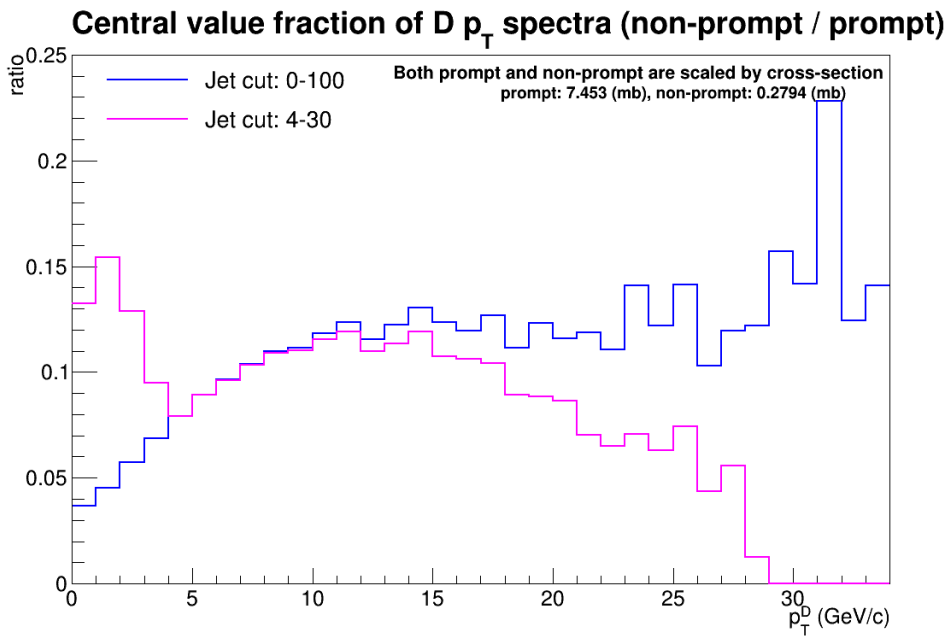

Figure 4.14 – Non-prompt over prompt D meson production for central values of D p_T spectra. Both prompt and non-prompt are scaled by their respective cross-sections (in millibar).

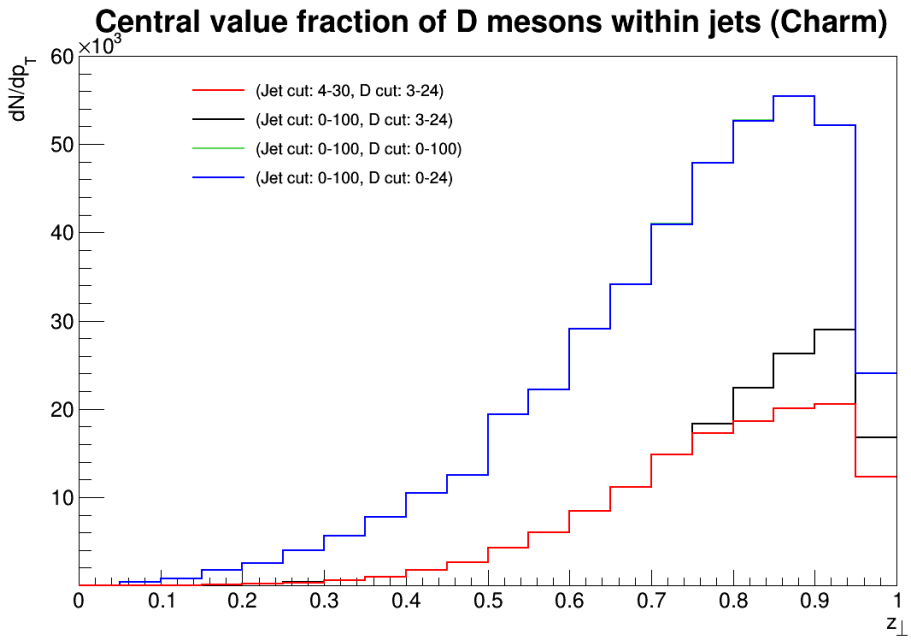

Figure 4.15 – Prompt D meson fraction in jets for different cuts. The red line represents a cut on in the jet **and** in the D meson spectra.

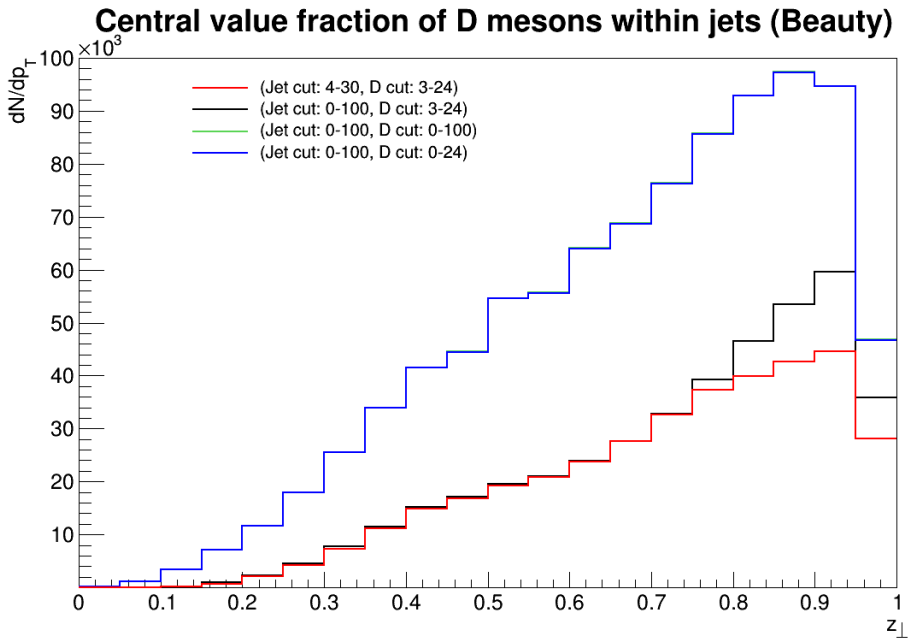

Figure 4.16 – Non-prompt D meson fraction in jets for different cuts. The red line represents a cut on in the jet **and** in the D meson spectra.

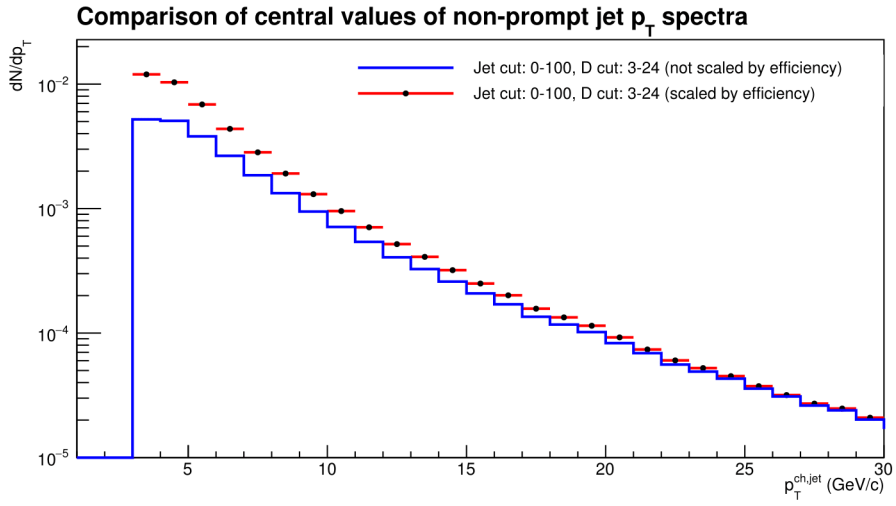

Figure 4.17 – Non-prompt central value of Cut 0 scaled and not scaled by efficiency.

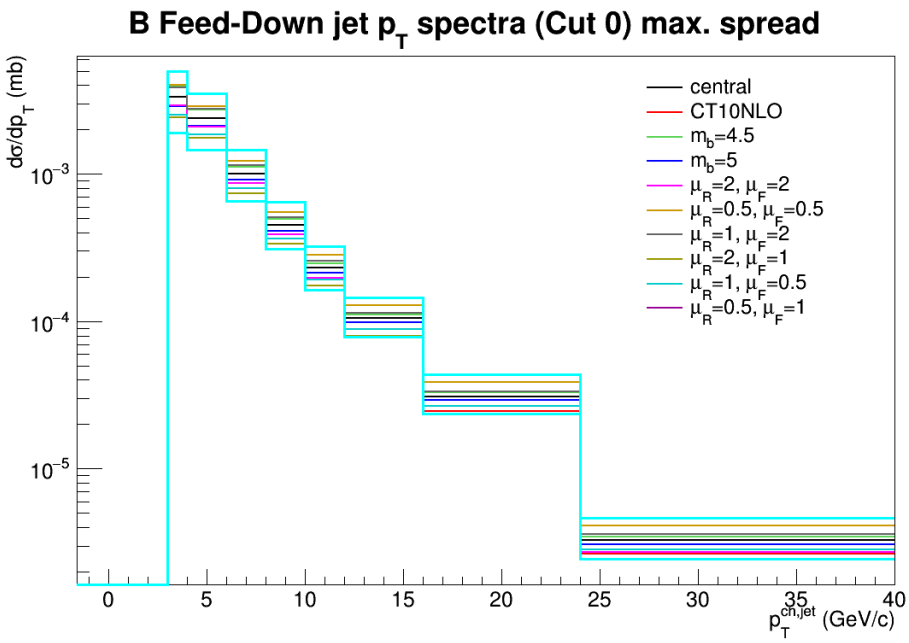

Figure 4.18 – Non-prompt jet p_T variations for Cut 0 scaled by the cross-section, with maximum variation band shown in teal.

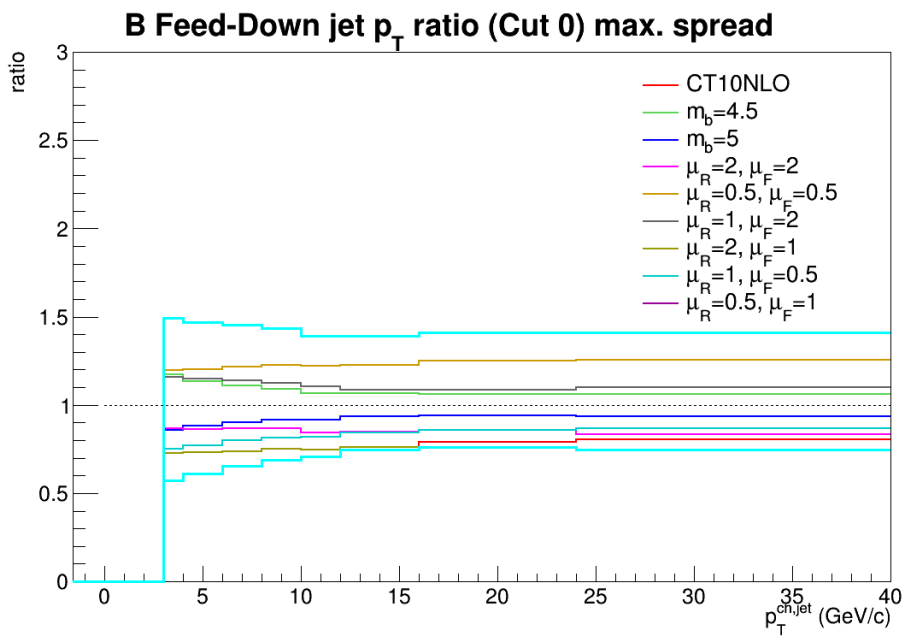

Figure 4.19 – Ratio for non-prompt jet p_T variations with respect to the central value for Cut 0. The maximum variation band is shown in teal.

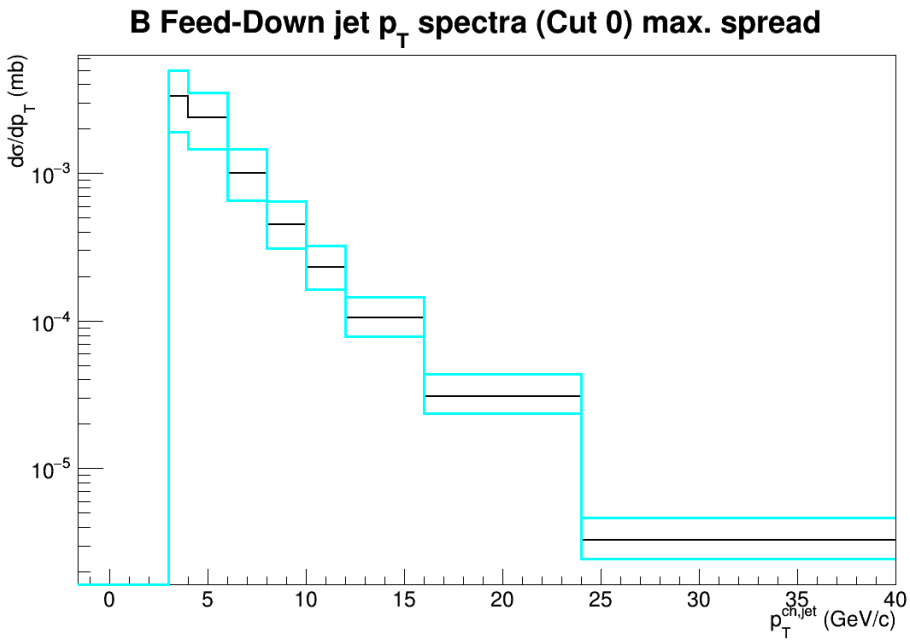

Figure 4.20 – Non-prompt jet p_T central value with maximum spread of the variations for Cut 0.

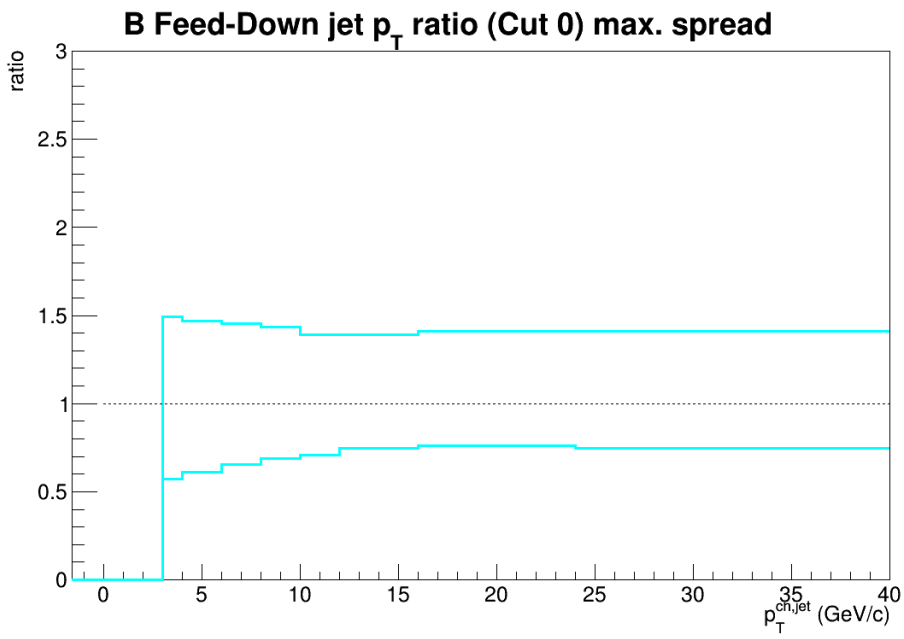

Figure 4.21 – Non-prompt jet p_T maximum spread ratio for Cut 0. The uncertainty is asymmetric.

Chapter 5

Conclusions

In this thesis I researched D-tagged jets in the ALICE experiment. I studied p-Pb collision simulations at $\sqrt{s_{NN}} = 5.02$ TeV. This is an important study since it provides a reference for Pb-Pb collisions where the quark-gluon plasma is created. The goal of the research was to study the uncertainties and effects on analysis cuts in prompt and non-prompt simulations. The effects on analysis cuts was studied by applying cuts in p_T ranges of either jet p_T or D p_T spectra. This was done for prompt (c→D) and non-prompt (b→B→D) simulation. To study the uncertainties in the simulation, multiple modifications on the starting conditions were applied, like a modification on quark mass or PDF. These modifications led to a spread in the variations with respect to the central value in the simulation. These effects by applying modifications and the effects on analysis cuts can be viewed in appendices A and B. To view more clearly what the effects on analysis cuts are, I plotted a ratio between the different cuts, which shows a clear decrease in D-jets close to the cuts (figures 4.9-4.12). This effect is stronger when looking at D p_T distributions than looking at jet p_T distributions. The reason for this is that in D p_T distributions, I cut on jet p_T spectra, which limits a large fraction of D p_T spectra. When looking at jet p_T distributions, I cut on D p_T spectra, which is only a part of the whole jet momentum (since the jet contains other particles than D mesons). Figures 4.13 and 4.14 show the ratio of non-prompt by prompt D mesons in jets, which have been scaled by their respective cross-section. From this we can see that at low p_T the fraction of non-prompt by prompt D mesons is rather low (around 10%). At high p_T, this ratio increases. Applying analysis cuts show that at high p_T the ratio is higher than if no cut is applied.

The effects on analysis cuts are clearly visible in figures 4.15 and 4.16, where we see the fraction of jet p_T carried by the D^* meson. Also visible is the difference of the amount of jets, which contain a high fraction of jet p_T carried by the D^* meson, between prompt and non-prompt simulation. These fractions change in the data analysis when we apply efficiencies.

Before the inclusive data (prompt+non-prompt) from ALICE can be compared with simulation we need to subtract the B feed-down from data. This B feed-down is a non-prompt simulation for Cut 0 (3-24 GeV/c) which has been scaled by efficiency and cross-section (figure 4.18). From figure 4.19 we can see the ratio for all the different variations with respect to the central value. In order to answer the question: "What are the systematic uncertainties for the D-tagged jet measurements?", we have to look at the maximum spread of all the variations of this B feed-down subtraction. This is is shown in figure 4.20 and 4.21. From this plot we see that the spread of the variations with respect to the central value is actually asymmetric. To get the systematic uncertainty from this, we look at the maximum spread. Table 4.1 shows the systematic uncertainty for the up, down and maximum spread.

The origin of these systematic uncertainties are widely discussed in this thesis. Applying analysis cuts and introducing modifications on the default starting values of the simulation lead to a variety of different simulations. The reason to cut the B feed-down

simulation at a p_T range 3-24 GeV/c is because it has to match the selection criteria used in the data analysis. These data cuts are necessary in order to get a right signal (section 4.3). We have seen that implementing this analysis cut has great consequences on the shape of the distribution and also the fraction of jet p_T carried by the D^* meson. As we can see, the modifications on the default starting values account for the systematic uncertainties visualized in figure 4.19, which is around 40-50%. These modifications are introduced since we do not know the exact values for the quark mass, renormalization, factorization and PDF. Determining more exact values of these modifications will directly result in smaller systematic uncertainties.

Chapter 6

Outlook and discussion

The next step in this research is to actually compare simulation with data. Since not all corrections are fully ready, the shown jet p_T spectrum is from data that is a preliminary first look. However, it is close enough to have a meaningful comparison with theory. And to estimate the effect of the non-prompt simulation systematic uncertainties in the B feed-down subtraction from the data. Figure 6.1 shows the comparison between data, which already has been B feed-down subtracted, and the central value of prompt simulation. In my research I was applying an analysis cut of 3-24 GeV/c, which corresponded to old data. The data that I show here is more recent and was cut at 3-36 GeV/c. Before I was able to compare my simulation to data, there needed to be some scaling. The data was scaled by $\frac{1}{BR \times Luminosity}$, where BR is the branching ratio (discussed in section 3.2), and luminosity in millibar. The simulation was scaled by the number of events, A_{Pb} (atomic number lead) and cross-section.

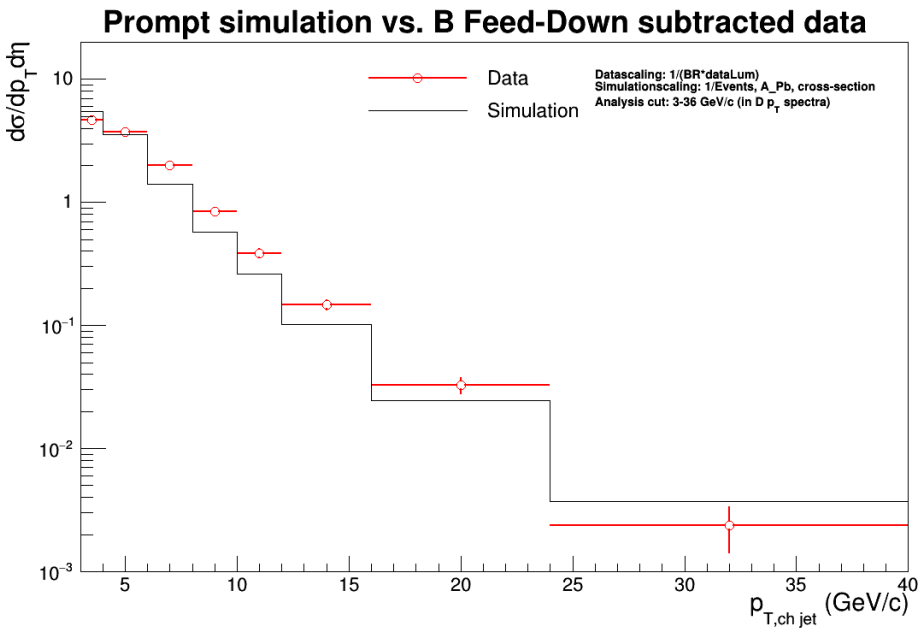

Figure 6.1 – The data here has been subtracted for the non-prompt simulation and is compared to the central value of the scaled prompt simulation for cut: 3-36 GeV/c.

As we can see from this figure, the central value of the simulation matches the data quite nicely. If we add all the variations however, we see a complete overlap between simulation and data. This is shown in figure 6.2

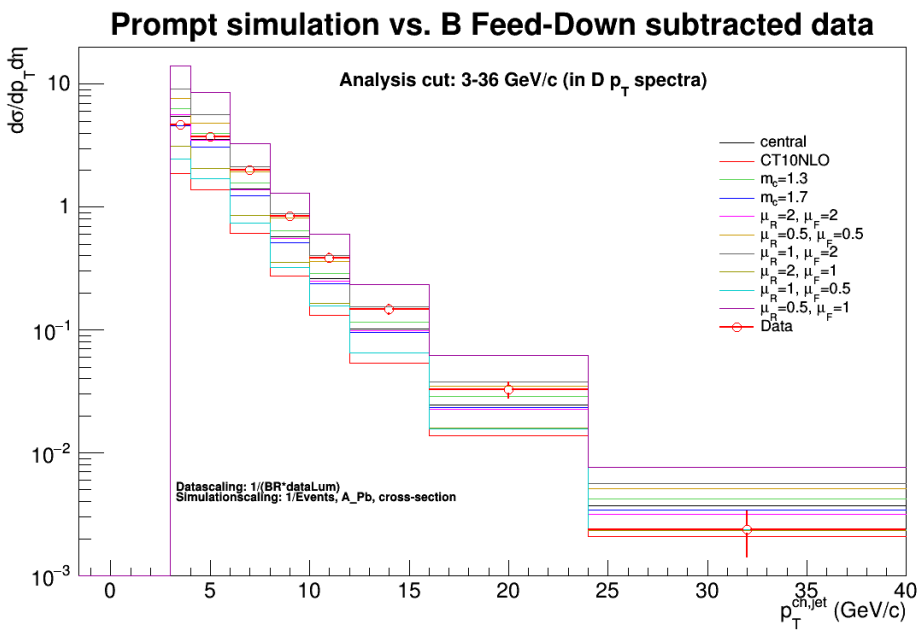

Figure 6.2 – Subtracted data compared to prompt simulation jet p_T spectra (cut 3-36 GeV/c). All the variations with respect to the central value of the simulation are shown, and overlaps with the data.

Figure 6.3 shows the feed-down fraction with uncertainties of non-prompt D^* jet p_T in the measured data. It is obtained by taking $\frac{data}{feed-down\ simulation}$. To find the final uncertainty, we need to multiply this feed-down fraction with the maximum uncertainties in the simulation (table 4.1). This final uncertainty is shown in table 6.1.

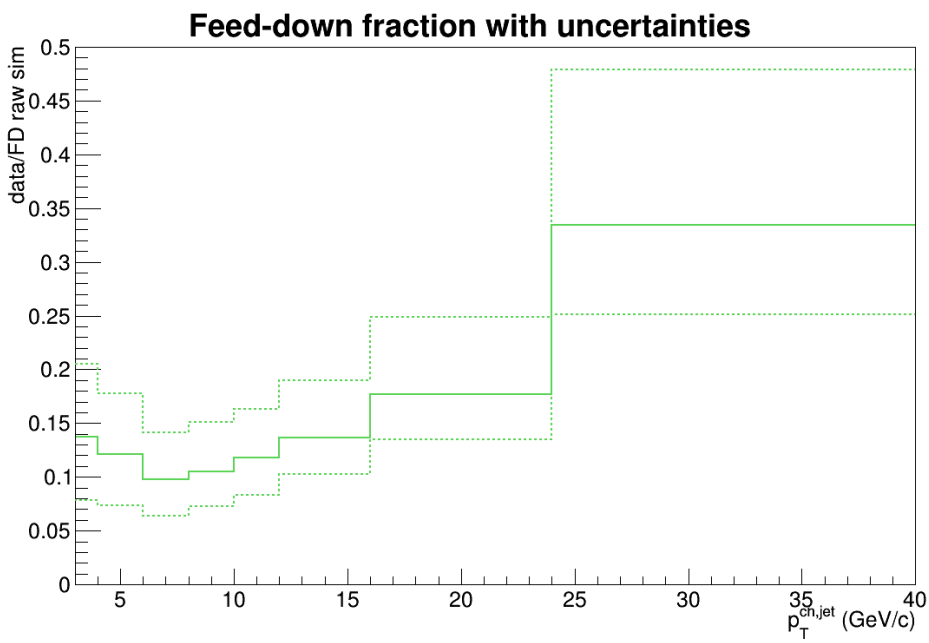

Figure 6.3 – B feed-down fraction of non-prompt D^* jet p_T in measured data. The dotted green lines represent the uncertainties in the feed-down fraction.

Table 6.1 – Table of the final uncertainties

B feed-down	Uncertainty (%)							
$p_T^{ch,jet}$ bin	3-4	4-6	6-8	8-10	10-12	12-16	16-24	24-40
Maximum	49	47	45	43	39	39	41	41
Feed-down fraction	14	12	10	11	12	14	18	33
Final uncertainty	7	6	5	5	5	5	7	14

Chapter 7

Acknowledgements

I would like to express my thanks to my daily thesis supervisor, Barbara Trzeciak, for always helping me and being patient with me when I had a seemingly endless stream of questions each week. I want to thank her for the help she provided understanding the theory and explaining the ROOT framework. Also I want to thank Cristina Bedda for helping me in the early stages of the research with the ROOT program. Also I would like to thank the QGP research group for the group meetings every week, making me aware that a good introduction of the story is one of the most important parts of a presentation.

Bibliography

[1] *Standard model* (2017), URL http://www.physik.uzh.ch/groups/serra/StandardModel.html.

[2] M. Strassler, *The strengths of the known forces* (2013), URL https://profmattstrassler.com/articles-and-posts/particle-physics-basics/the-known-forces-of-nature/the-strength-of-the-known-forces/.

[3] M. E. Peskin and D. V. Schroeder, *An Introduction to Quantum Field Theory* (Avalon Publishing, 2015), student economy edition ed., ISBN 0813350190, 9780813350196.

[4] W. Florkowski, *Phenomenology of Ultra-Relativistic Heavy-Ion Collisions* (World Scientific Publishing Company, 2010), 1st ed., ISBN 978-9814280662.

[5] D. C. Giancoli, *Physics: Principles with Applications* (Prentice Hall, 1995), 4th ed.

[6] J. P. Preskill, *The discovery of asymptotic freedom*, URL http://www.theory.caltech.edu/~preskill/Nobel2004_JP.pdf.

[7] S. Oomen, *Testing the pALPIDE v2 chip and researching module testing methods for the ALICE ITS upgrade* (2016).

[8] E. L. Wright, *Frequently asked questions in cosmology* (2013), URL http://www.astro.ucla.edu/~wright/cosmology_faq.html#BBevidence.

[9] *Timeline of the universe*, URL http://planck.cf.ac.uk/science/timeline/universe/inflation.

[10] A. Grelli, *Probing the early universe in the laboratory*, lecture Utrecht University (2015).

[11] T. Nayak, RHIC news (2008), URL https://www.bnl.gov/rhic/news/040808/story3.asp.

[12] *The Large Hadron Collider* (2017), URL http://home.cern/topics/large-hadron-collider.

[13] *LHC is back* (2010), URL http://people.physics.tamu.edu/kamon/research/refColliders/LHC/LHC_is_back.html.

[14] *LHC experiments* (2017), URL https://home.cern/about/experiments.

[15] *Heavy-ion physics with the ALICE experiment at the CERN Large Hadron Collider*, URL http://rsta.royalsocietypublishing.org/content/370/1961/917.

[16] F. Antorini, Nuclear Instruments and Methods in Physics Research Section A: Accelerators, Spectrometers, Detectors and Associated Equipment **511** (2003).

[17] E. M. Henley and A. Garca, *Subatomic Physics* (World Scientific Publishing Company, 2007), 3rd ed., ISBN 981-270-056-0.

[18] *The ALICE Time Projection Chamber (TPC)*, URL http://aliceinfo.cern.ch/Public/en/Chapter2/Chap2_TPC.html.

[19] *The ALICE Time of Flight Detector*, URL http://aliceinfo.cern.ch/Public/en/Chapter2/Chap2_TOF.html.

[20] *CERN LHC creates temperatures 100,000 times hotter than the center of the sun* (2011), URL http://www.dailygalaxy.com/my_weblog/2011/06/cern-lhc-creates-temperatures-1000-times-hotter-than-center-of-sun.html.

[21] B. Andersson, G. Gustafson, G. Ingelman, and T. Sjörstrand, PHYSICS REPORTS (Review Section of Physics Letters) **97** (1983).

[22] *Jet-like correlations* (2012), URL https://drupal.star.bnl.gov/STAR/pwg/jet-correlations.

[23] *Premire S*, URL http://lfrancope.edu.pe/moodle/mod/glossary/print.php?id=343&mode=date&hook=&sortkey=CREATION&sortorder=asc&offset=10.

[24] S. Aiola, F. F. Colamaria, A. Rossi, A. C. O. da Silva, and B. A. Trzeciak, Preliminary figures for Quark Matter (2017).

[25] B. A. Trzeciak, *Heavy-flavour production with the ALICE experiment at the LHC*, private communication (2016).

[26] M. Cacciari, G. P. Salam, and G. Soyez, Journal of High Energy Physics **6** (2008).

[27] *Renormalization*, URL https://ncatlab.org/nlab/show/renormalization#Renormalization.

[28] J. Feltesse, *Introduction to Parton Distribution Functions* (2010), URL http://www.scholarpedia.org/article/Introduction_to_Parton_Distribution_Functions.

Chapter 8

Syllabus

- **Hadrons:** Subatomic particles (protons and neutrons) that are subject to the strong force.
- **Parton:** A particle (quark or gluon) that is a constituent of hadrons.
- **Deconfinement:** The moment when quarks and gluons are no longer confined to hadrons and are free to move independent.
- **Quark-gluon plasma:** A state of matter with a very high temperature and/or density where quarks and gluons are deconfined and form a plasma.
- **Deep inelastic scattering:** A process used to probe the insides of hadrons. The kinetic energy of an incident particle is not conserved.
- **Thermal equilibrium:** A state of a system where all parts have an equal temperature.
- **Decoupling:** The development of a system where particles fall out of thermal equilibrium with each other.
- **Initial hard scattering:** Initial period in heavy-ion collisions where the particles collide.
- **Coalescence:** The merging of two particles into one resulting from mutual assimilation.
- **Vertexing:** The detection of vertices in the tracks of particles.
- **Branching ratio:** The ratio of the number of particles decaying by a particular decay mode to the number decaying in total.
- **Transverse momenta ($\mathbf{p}_T$):** The component of momentum transverse (i.e. perpendicular) to the beam line.
- **Beam line:** The trajectory of the beam of accelerated particles.

Appendices

Appendix A

Non-prompt spectra

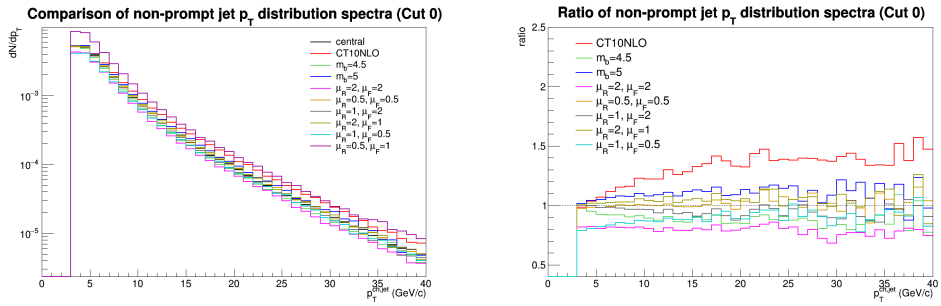

(a) Comparison of non-prompt spectra with different modifications.

(b) Ratio of non-prompt spectra with respect to the central value.

Figure A.1 – Comparison and ratio of jet p_T distributions: Cut 0 (D p_T cut: 3-24 GeV/c).

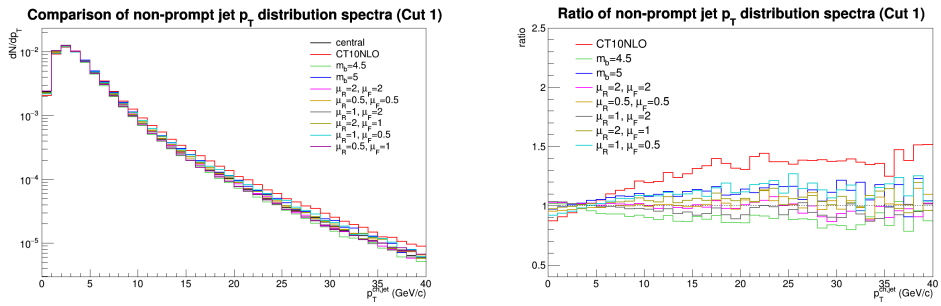

(a) Comparison of non-prompt spectra with different modifications.

(b) Ratio of non-prompt spectra with respect to the central value.

Figure A.2 – Comparison and ratio of jet p_T distributions: Cut 1 (D p_T cut: 0-100 GeV/c).

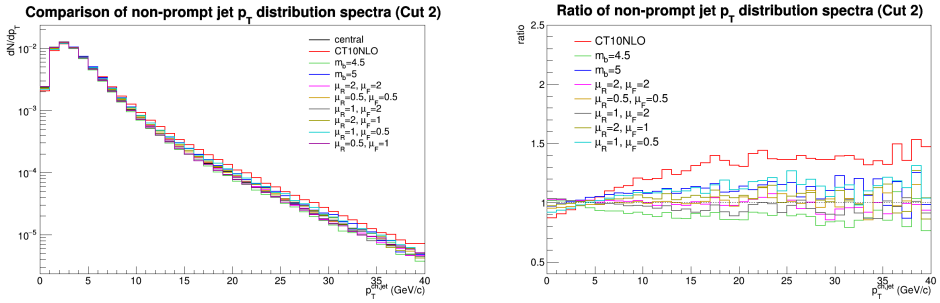

(a) Comparison of non-prompt spectra with different modifications.

(b) Ratio of non-prompt spectra with respect to the central value.

Figure A.3 – Comparison and ratio of jet p_T distributions: Cut 2 (D p_T cut: 0-24 GeV/c).

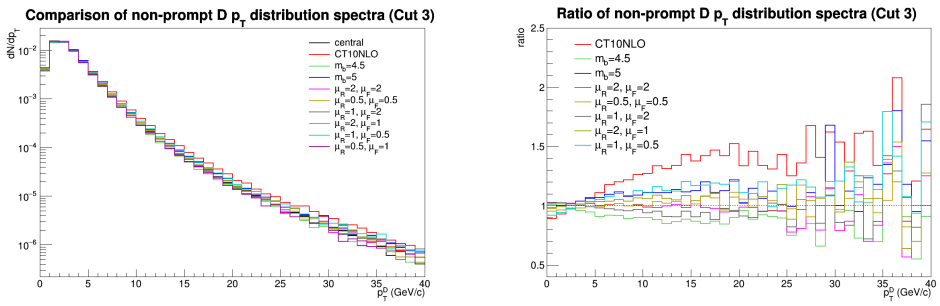

(a) Comparison of non-prompt spectra with different modifications.

(b) Ratio of non-prompt spectra with respect to the central value.

Figure A.4 – Comparison and ratio of D p_T distributions: Cut 3 (jet p_T cut: 0-100 GeV/c).

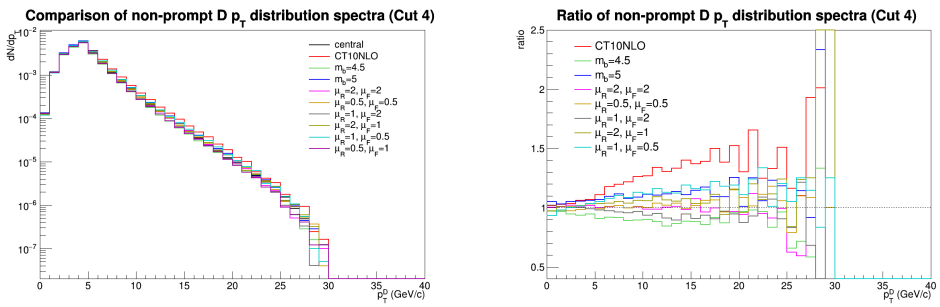

(a) Comparison of non-prompt spectra with different modifications.

(b) Ratio of non-prompt spectra with respect to the central value.

Figure A.5 – Comparison and ratio of D p_T distributions: Cut 4 (jet p_T cut: 4-30 GeV/c).

Appendix B

Prompt spectra

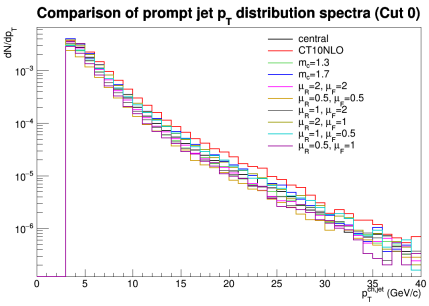

(a) Comparison of prompt spectra with different modifications.

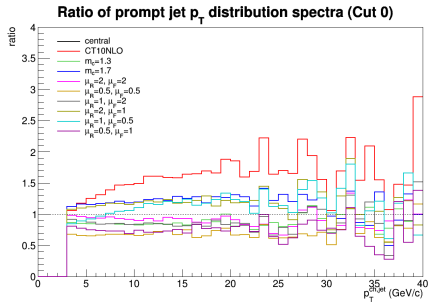

(b) Ratio of prompt spectra with respect to the central value.

Figure B.1 – Comparison and ratio of jet p_T distributions: Cut 0 (D p_T cut: 3-24 GeV/c).

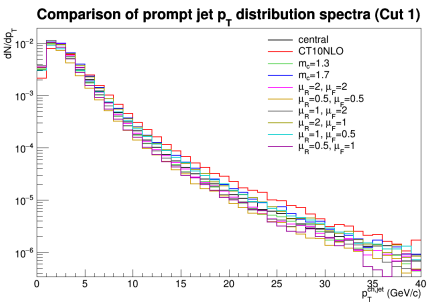

(a) Comparison of prompt spectra with different modifications.

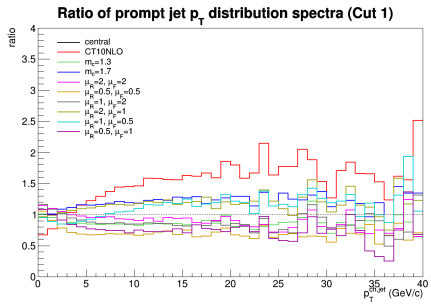

(b) Ratio of prompt spectra with respect to the central value.

Figure B.2 – Comparison and ratio of jet p_T distributions: Cut 1 (D p_T cut: 0-100 GeV/c).

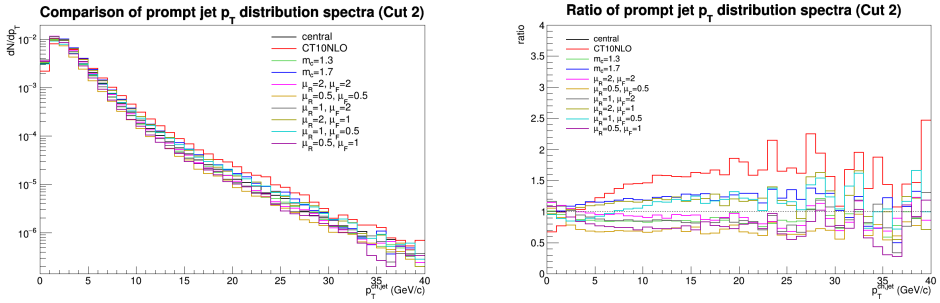

(a) Comparison of prompt spectra with different modifications.

(b) Ratio of prompt spectra with respect to the central value.

Figure B.3 – Comparison and ratio of jet p_T distributions: Cut 2 (D p_T cut: 0-24 GeV/c).

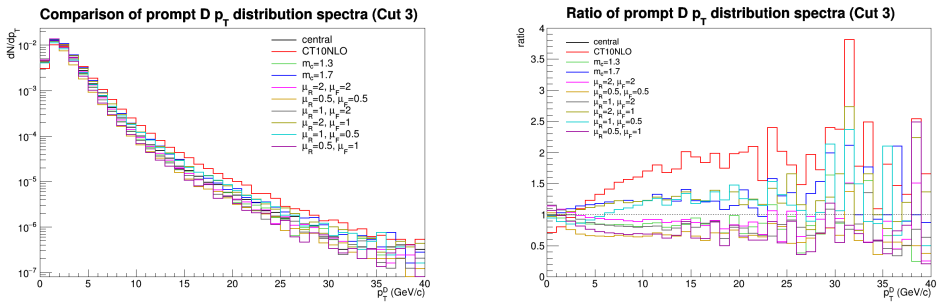

(a) Comparison of prompt spectra with different modifications.

(b) Ratio of prompt spectra with respect to the central value.

Figure B.4 – Comparison and ratio of D p_T distributions: Cut 3 (jet p_T cut: 0-100 GeV/c).

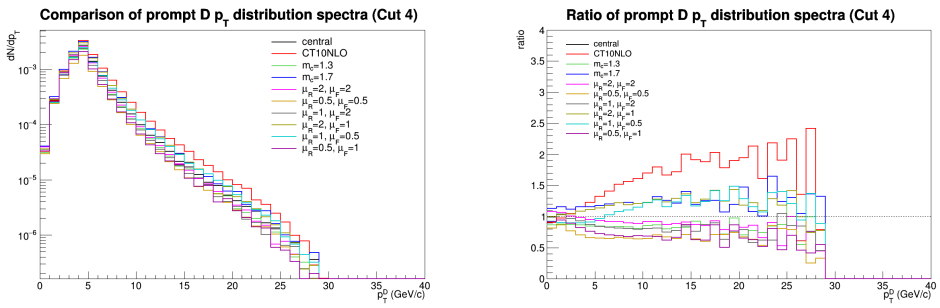

(a) Comparison of prompt spectra with different modifications.

(b) Ratio of prompt spectra with respect to the central value.

Figure B.5 – Comparison and ratio of D p_T distributions: Cut 4 (jet p_T cut: 4-30 GeV/c).